Computational Mechanics (2023) 71:71–88
https://doi.org/10.1007/s00466-022-02217-3

ORIGINAL PAPER

Computational multi-phase convective conjugate heat transfer on overlapping meshes: a quasi-direct coupling approach via Schwarz alternating method

Ze Zhao[1] · Qiming Zhu[1] · Anand Karuppiah[2] · Michael Stuebner[2] · Jim Lua[2] · Nam Phan[3] · Jinhui Yan[1]

Received: 10 June 2022 / Accepted: 20 July 2022 / Published online: 9 August 2022

Abstract
We present a new computational framework to simulate the multi-phase convective conjugate heat transfer (CHT) problems emanating from realistic manufacturing processes. The paper aims to address the challenges of boundary-fitted and immersed boundary approaches, which cannot simultaneously achieve fluid-solid interface accuracy and geometry-flexibility in simulating this class of multi-physics systems. The method development is built on a stabilized Arbitrary Lagrangian-Eulerian (ALE)-based finite element thermal multi-phase formulation, which is discretized by overlapping one boundary-fitted mesh and non-boundary-fitted mesh with a quasi-direct coupling approach via Schwarz alternating method. The framework utilizes a volume-of-fluid (VoF)-based multi-phase flow model coupled with a thermodynamics model with phase transitions to capture the conjugate heat transfer between the solid and multi-phase flows and the multi-stage boiling and condensation phenomena. The quasi-direct coupling approach allows the exact and automatic enforcement of temperature and heat-flux compatibility at the fluid-solid interface with large property discontinuities. From the perspective of method development, the proposed framework fully exploits boundary-fitted approach's strength in resolving fluid-solid interface and boundary layers and immersed boundary approach's geometry flexibility in handling moving objects while circumventing each individual's limitations. From the perspective of industry applications, such as water quenching processes, the resulting model can enable accurate temperature prediction directly from process parameters without invoking the conventional empirical heat transfer coefficient (HTC)-based approach that requires intensive calibration. We present the mathematical formulation and numerical implementation in detail and demonstrate the claimed features of the proposed framework through a set of benchmark problems and real-world water quenching processes. The accuracy of the proposed framework is carefully assessed by comparing the prediction with other computational results and experimental measurements.

Keywords Advanced manufacturing · Computational fluid dynamics · Overlapping meshes · Finite element method

1 Introduction

The term "conjugate heat transfer (CHT)" [1] describes a coupled solid-fluid thermal system, where the heat transfer in the solid is heavily influenced by the surrounding fluid. Typically, heat conduction dominates in the solid domain, and convection dominates in the fluid domain. Convective CHT systems are a unique type of multi-physics system. It possesses the features of both bulk-coupled multi-physics systems: the coupling of physical components occurs at every spatial point of the problem domain through source terms or constitutive relations (e.g., radiation hydrodynamics), and interface-coupled multi-physics systems: the physics coupling occurs through an idealized interface or a narrow buffer zone through boundary conditions (e.g., fluid-structure interaction). More specifically, in convective CHT problems, the flow and temperature fields are coupled both in the fluid domain and through the fluid-solid interface, where the no-slip flow boundary condition, temperature, and heat flux compatibility need to be satisfied simultaneously. Convective conjugate heat transfer exists in a wide range of heat treatment and composite manufacturing processes that are

✉ Jinhui Yan
yjh@illinois.edu

[1] Department of Civil and Environmental Engineering, University of Illinois at Urbana-Champaign, Champaign, IL, USA

[2] Global Engineering and Materials, Inc, Princeton, USA

[3] Naval Air Systems Command, Maryland, USA

used by industry to obtain specific mechanical properties of metallic and composite structures. One representative example is the water quenching process [2]. In water quenching, rapid and non-uniform cooling processes can generate undesired residual stress and distortion, which are detrimental to the structure functionality and even cause structural failure. Predicting the spatiotemporal temperature field to assess the resulting residual stress and distortion of quenched parts has been one of the most critical research areas in heat treatment processes. However, this task is challenging due to the multi-scale and multi-physics process that includes the strong coupling of thermal, flow, and mechanical interactions [3]. The convective CHT problems arising from real-world heat treatment/manufacturing processes of large-scale components impose grand challenges on computational mechanics. The main challenge stems from the fluid-solid interface with complex geometry and large property ratios, leading to several critical issues pertinent to mesh flexibility, enforcing boundary conditions, and resolving boundary layers.

In computational fluid dynamics (CFD) and fluid-structure interaction (FSI), there are two types of methods for handling fluid-solid interface: boundary-fitted and immersed boundary methods. Each method has its strength and weakness. On the one hand, boundary-fitted method [4–7] is more accurate than immersed boundary method in resolving fluid-solid interface and associated boundary layer phenomena, and the temperature and heat flux compatibility can be automatically satisfied if a monolithic coupling approach is adopted. However, they require tremendous effort in pre-processing to generate the conforming mesh of the fluid-solid interface and volumetric meshes for fluid and solid sub-domains. They also necessitate sophisticated mesh motion and even remeshing techniques if the solid undergoes significant motion or triggers topology changes in the fluid domain [8–10]. On the other hand, immersed boundary method [11], such as finite cell method [12–14], shifted boundary method [15–19], cutFEM [20], immersed-particle method [21–25], immersed finite element [26–31], and immersogeometric method [32–35] offers great mesh flexibility in pre-processing and handling moving objects. However, the non-boundary-fitted nature leads to lower resolution of the fluid-solid interface and boundary layers, which can be problematic in some multi-phase convective CHT problems, such as those in water quenching, where rapid phase transition (e.g., evaporation and condensation) takes place at the fluid-solid interface. Besides, it is burdensome to enforce the heat flux compatibility across the fluid-solid interface with large property discontinuity, especially if linear spatial discretization is employed.

The objective of this paper is to develop an effective multi-phase convective CHT framework to address the challenges mentioned above, and deploy it to water quenching processes of complex structures. The proposed framework aims to take boundary-fitted method's advantages in resolving boundary layers and enforcing heat flux compatibility and immersed boundary method's advantage in mesh flexibility of handling moving objects while overcoming their weakness. The essence of the framework is built upon an overlapping mesh (also called composite, overset, or Chimera mesh in the literature [36–41]) technique. An overlapping mesh consists of multiple meshes that occupy a problem domain and overlap where they meet. Interpolation or other numerical techniques at overlapping boundaries are performed to ensure the continuity of physical variables across the different component meshes. Overlapping meshes have been used to solve CFD and FSI problems involving moving objects. Despite considerable research and applications of overlapping meshes in the literature, most are based on structured meshes combined with finite difference or finite volume methods and primarily used for the single-phase CFD simulations in aerospace applications [42–45]. Developing an overlapping mesh technique using finite element method to solve the conjugate CHT problems involving multi-phase flows with phase transition is lacking. An effective multi-phase convective CHT model is in high demand in the heat treatment and composite manufacturing industries, which currently rely on the empirical models by calibrating heat transfer coefficients due to the complexity of the multi-physics and structural geometry.

In this paper, we propose an unstructured overlapping mesh technique with the Schwarz alternating method to solve the multi-phase convective CHT problems with phase transitions. The overlapping mesh technique consists of two overlapping unstructured meshes. One unstructured mesh, denoted by **Mesh 1**, which contains the entire solid domain and partial fluid domain, utilizes a boundary-fitted approach integrated with Arbitrary-Lagrangian-Eulerian (ALE) technique to handle moving fluid-solid interface and overlapping boundaries. Another unstructured mesh, denoted by **Mesh 2**, which contains the complementary fluid domain, utilizes a non-boundary-fitted discretization of overlapping boundaries, and a Schwarz alternating method is adopted to ensure the continuities of flow/temperature fields and the heat flux compatibility. Since the fluid-solid interface is explicitly resolved, the flow/temperature boundary condition and boundary layer behavior are captured more accurately. The technique also retains the mesh flexibility of the immersed boundary method by applying it to a fluid-fluid interface (overlapping boundary) rather than a fluid-solid interface to circumvent the challenges associated with large property ratios and boundary conditions. The unstructured overlapping mesh technique is deployed to a stabilized formulation of thermal multi-phase flows. A volume-of-fluid (VoF)-based evaporation/condensation model is augmented to handle the phase transitions. The proposed multi-physics framework is solved in a quasi-direct coupling strategy between **Mesh 1** and **Mesh 2** with a multi-stage predictor-corrector iterative

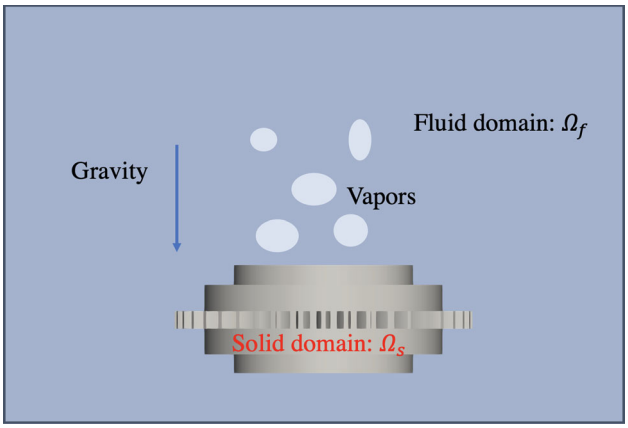

Fig. 1 A multi-phase convective conjugate heat transfer (CHT) system during a water quenching process

scheme and a generalized-α method for time integration. The coupling strategy is analogous to the approaches proposed in [46] for solving fluid-structure interaction problems with moving meshes. That is, within each nonlinear iteration, the coupled heat and fluid mechanics equations defined in **Mesh 1** are solved in a monolithic fashion to ensure the exact enforcement of temperature and flux boundary conditions. Then, the boundary conditions on overlapping boundaries are passed to **Mesh 2** to solve the flow and temperature equations defined there. Such iterations continue until the residuals of all the equations of both meshes are reduced below the convergence criteria.

The paper is structured as follows. In Sect. 2, we present the computational framework of multi-phase CHT problems. All the details, including the governing equations, semi-discrete formulation, time integration, Schwarz alternating method on overlapping unstructured meshes, quasi-direct coupling, and linear solver, are thoroughly described. Two verification examples and two realistic water quenching simulations with stationary and moving metallic structures are presented in Sect. 3 to demonstrate the proposed framework's accuracy and predictive capability. The accuracy is assessed by comparing the predicted results with available experimental data and the predictions from the single mesh-based boundary-fitted method. Conclusions are made in Sect. 4.

2 Computational Framework

2.1 Governing equations and phase transition model

Figure 1 depicts a multi-phase (vapor-liquid) convective CHT system during a water quenching process, involving multi-phase flows, thermodynamics, and phase transitions. The flows are assumed to be incompressible in individual fluid phase except the vapor-liquid interface, where boiling and condensation introduces compressibility. We employ an Arbitrary-Lagrangian-Eulerian (ALE) technique to solve the system on moving domains. For the sake of clarity, we utilize subscripts $(\cdot)_f$, $(\cdot)_s$, and $(\cdot)_m$ to differentiate the quantities associated with the fluid domain, solid domain, and the mesh, respectively. In the fluid domain, $(\cdot)_f$ can be set to $(\cdot)_l$ and $(\cdot)_v$ to differentiate the liquid and vapor phases. With the above definitions, the physical behaviors of the multi-phase convective CHT system can be described by the following partial differential equations.

$$R_f^C := \frac{\partial \rho_f}{\partial t} + (\boldsymbol{u} - \boldsymbol{u}_m) \cdot \nabla \rho_f + \rho_f \nabla \cdot \boldsymbol{u} = 0 \quad \text{in} \quad \Omega_f \tag{1}$$

$$\boldsymbol{R}_f^M := \rho_f \left[\frac{\partial \boldsymbol{u}}{\partial t} + (\boldsymbol{u} - \boldsymbol{u}_m) \cdot \nabla \boldsymbol{u} - \boldsymbol{g} \right] - \nabla \cdot \boldsymbol{\sigma} = \boldsymbol{0} \quad \text{in} \quad \Omega_f \tag{2}$$

$$R_f^T := \frac{\partial H_f}{\partial t} + (\boldsymbol{u} - \boldsymbol{u}_m) \cdot \nabla H_f + H_f (\nabla \cdot \boldsymbol{u}) - \nabla \cdot (\kappa_f \nabla T_f) = 0 \quad \text{in} \quad \Omega_f \tag{3}$$

$$R_f^\phi := \rho_v \frac{\partial \phi}{\partial t} + \rho_v (\boldsymbol{u} - \boldsymbol{u}_m) \cdot \nabla \phi + \rho_v \phi (\nabla \cdot \boldsymbol{u}) - \dot{m} = 0 \quad \text{in} \quad \Omega_f \tag{4}$$

$$R_s^T := \rho_s c_s \frac{\partial T_s}{\partial t} - \nabla \cdot (\kappa_s \nabla T_s) = 0 \quad \text{in} \quad \Omega_s \tag{5}$$

$$\boldsymbol{u} - \boldsymbol{u}_g = \boldsymbol{0} \quad \text{on} \quad \Gamma_{fs} \tag{6}$$

$$T_s - T_f = 0 \quad \text{on} \quad \Gamma_{fs} \tag{7}$$

$$\kappa_s \boldsymbol{n}_s \cdot \nabla T_s + \kappa_f \boldsymbol{n}_f \cdot \nabla T_f = 0 \quad \text{on} \quad \Gamma_{fs} \tag{8}$$

where Ω_f, Ω_s, and Γ_{fs} denote the fluid sub-domain, solid sub-domain, and fluid-solid interface, respectively. The physical meaning of each equation is given as follows.

- In the fluid sub-domain, Eqs. 1 and 2 represent the conservation laws of mass and momentum (Navier-Stokes equations), where $\boldsymbol{\sigma} = -p\boldsymbol{I} + 2\mu_f[\nabla^S \boldsymbol{u} - \frac{1}{3}(\nabla \cdot \boldsymbol{u})\boldsymbol{I}]$ is the stress, where $\boldsymbol{I}$ is an identity matrix, ∇^S is the symmetric gradient operator, $\boldsymbol{u}$ and p denote the fluid velocity and pressure unknowns, $\boldsymbol{g}$ is the gravitational acceleration, ρ_f and μ_f are the fluid density and dynamics viscosity, respectively. Eq. 3 represents the conservation of energy, in which κ_f is conductivity of liquid and H is the enthalpy. H_f is defined as $H_v = \rho_v c_v (T_f - T_0) + \rho_v L$ in the vapor phase and $H_l = \rho_l c_l (T_f - T_0)$ in the liquid phase, where T_f is the fluid temperature, c_l and c_v are the heat capacities of liquid and vapor phases, T_0 is a reference temperature, and L is the latent of vaporization. Eq. 4 represents the volume of fluid (VoF) transport equation, in which ϕ denotes the vapor fraction and $\dot{m}$ represents the phase transition model, which will be specified next. In the fluid domain, all the equations are written in the ALE form with $\boldsymbol{u}_m$ representing the mesh velocity.
- In the solid sub-domain Ω_s, Eq. 5 represents the heat conduction, in which T_s is the solid temperature, ρ_s, c_s, and

κ_s are the solid density, heat capacity, and conductivity, respectively.

- On fluid-solid interface Γ_{fs}, Eqs. 6, 7, and 8 represent the no-slip ($\boldsymbol{u}_g$ is the velocity of the solid), heat, and flux boundary conditions, where $\boldsymbol{n}_f$ and $\boldsymbol{n}_s$ are the unit normal vector on the fluid-solid interface ($\boldsymbol{n}_s = -\boldsymbol{n}_f$).

We make use of a mixture multi-phase flow model, meaning any mechanical/thermal property χ_f in the fluid domain is given by the linear combination of the corresponding liquid property and vapor property, namely,

$$\chi_f = \phi\chi_v + (1-\phi)\chi_l \tag{9}$$

Water quenching processes involve rapid boiling and condensation phenomena. To this end, we employ the following evaporation-condensation model, adopted from [47,48], to simulate the phase transitions between liquid and vapor phases. This model takes care of the phase transitions near the fluid-solid interface as well as inside the fluid domain.

$$\dot{m} = \begin{cases} C_{evap}(1-\phi)\rho_l \frac{T_f - T_{sat}}{T_{sat}}, & T_f > T_{sat} \\ C_{cond}\phi\rho_v \frac{T_f - T_{sat}}{T_{sat}}, & T_f \leq T_{sat} \end{cases} \tag{10}$$

where C_{evap} and C_{cond} are the evaporation and condensation coefficients, T_{sat} is the saturation temperature. The values of C_{evap} and C_{cond} depend on the mean Sauter diameter of the vapor bubble, phase fraction, and fluid properties. Generally, these two coefficients need to be evaluated experimentally for a given quenching medium. Following the guidelines provided by [47], we set $C_{evap} = 1$ and $C_{cond} = 0.1$ for the water quenching processes considered in this paper.

With the above the VoF mixture and evaporation models, the conservation laws of mass and enthalpy are further modified such that all physical unknowns of the mathematical model are based on fluid velocity, pressure, vapor fraction, and temperature. Firstly, substituting $\rho_f = \phi\rho_v + (1-\phi)\rho_l$ (based on Eq. 9) and the VoF transport equation (Eq. 4) into the mass conservation equation (Eq. 1) leads to

$$R_f^C := \nabla\cdot\boldsymbol{u} - \left(\frac{\dot{m}}{\rho_v} - \frac{\dot{m}}{\rho_l}\right) = 0 \tag{11}$$

Secondly, substituting $H_f = \phi H_v + (1-\phi)H_l$ (based on Eq. 9) and the VoF transport equation (Eq. 4) into the enthalpy conservation equation (Eq. 3) leads to

$$R_f^T =: \rho_f c_f\left[\frac{\partial T_f}{\partial t} + (\boldsymbol{u}-\boldsymbol{u}_m)\cdot\nabla T_f\right] - \nabla\cdot(\kappa_f\nabla T_f) - S_e = 0 \tag{12}$$

where S_e is a source term representing the phase transitions and defined as

$$S_e = [(c_l - c_v)(T - T_0) - L]\,\dot{m} \tag{13}$$

2.2 Semi-discrete formulation

We employ a stabilized finite element method to solve the partial differential equations of the multi-phase convective CHT system defined in the previous section. Besides, a residual-based discontinuity capturing technique [49,50] is augmented to handle the strong thermal property jump, and a weak enforcement of essential boundary conditions [51] (weak BC) is adopted to impose the no-slip flow boundary condition defined in Eq. 6.

In the fluid sub-domain Ω_f, let $\mathcal{V}_f$ denote the trial function space for unknown fluid velocity $\boldsymbol{u}$, pressure p, volume fraction ϕ, and fluid temperature T_f. $\mathcal{W}_f$ denotes the test function space for the momentum, continuity, enthalpy, and volume fraction equations. In the solid sub-domain Ω_s, let $\mathcal{V}_s$ denote the trial function space for unknown solid temperature T_s, and $\mathcal{W}_s$ denote the test function space for the heat conduction equation. With the above definitions, the stabilized formulation augmented with discontinuity capturing and weak BC techniques for the multi-phase convective CHT system is stated as: $\forall\{\boldsymbol{w}, q, \zeta, \eta_f\} \in \mathcal{W}_f$ and $\eta_s \in \mathcal{W}_s$, find $\{\boldsymbol{u}, p, \phi, T_f\} \in \mathcal{V}_f$ and $T_s \in \mathcal{V}_s$, such that

$$\begin{aligned} &W^G\left(\{\boldsymbol{w}, q, \zeta, \eta_f, \eta_s\}; \{\boldsymbol{u}, p, \phi, T_f, T_s\}\right) \\ &+ W^{stab}\left(\{\boldsymbol{w}, q, \zeta, \eta_f\}; \{\boldsymbol{u}, p, \phi, T_f\}\right) \\ &+ W^{bc}\left(\{\boldsymbol{w}, q\}; \{\boldsymbol{u}, p\}\right) = 0 \end{aligned} \tag{14}$$

The meaning of each component is specified as follows.

- W^G represents the Gakerlin formulation of the multi-phase convective CHT problem, defined as

$$\begin{aligned} &W^G\left(\{\boldsymbol{w}, q, \zeta, \eta_f, \eta_s\}; \{\boldsymbol{u}, p, \phi, T_f, T_s\}\right) \\ &= \int_{\Omega_f} \boldsymbol{w}\cdot\rho_f\left[\frac{\partial \boldsymbol{u}}{\partial t} + (\boldsymbol{u}-\boldsymbol{u}_m)\cdot\nabla\boldsymbol{u} - \boldsymbol{g}\right] d\Omega \\ &+ \int_{\Omega_f} \nabla\boldsymbol{w} : \boldsymbol{\sigma}\, d\Omega + \int_{\Omega_f} q\left[\nabla\cdot\boldsymbol{u} - \dot{m}\left(\frac{1}{\rho_v} - \frac{1}{\rho_l}\right)\right] d\Omega \\ &+ \int_{\Omega_f} \eta_f\left\{\rho_f c_f\left[\frac{\partial T_f}{\partial t} + (\boldsymbol{u}-\boldsymbol{u}_m)\cdot\nabla T_f\right] - S_e\right\} d\Omega \\ &+ \int_{\Omega_f} \nabla\eta_f\cdot\kappa_f\nabla T_f\, d\Omega \\ &+ \int_{\Omega_f} \zeta\left\{\rho_v\left[\frac{\partial\phi}{\partial t} + (\boldsymbol{u}-\boldsymbol{u}_m)\cdot\nabla\phi + \phi\nabla\cdot\boldsymbol{u}\right] - \dot{m}\right\} d\Omega \\ &+ \int_{\Omega_s} (\eta_s\rho_s c_s\frac{\partial T_s}{\partial t} + \nabla\eta_s\cdot\kappa_s\nabla T_s) d\Omega \end{aligned} \tag{15}$$

- W^{stab} represents the stabilized method and is defined as

$$
\begin{aligned}
&W^{stab}\left(\{\boldsymbol{w}, q, \zeta, \eta_f\}; \{\boldsymbol{u}, p, \phi, T_f\}\right) \\
&= \int_{\Omega_f} \tau_f \left[(\boldsymbol{u} - \boldsymbol{u}_m)\cdot\nabla\boldsymbol{w} + \frac{\nabla q}{\rho_f}\right]\cdot \boldsymbol{R}_f^M \, d\Omega \\
&+ \int_{\Omega_f} \tau_C \rho_f (\nabla\cdot\boldsymbol{w}) R_f^C d\Omega \\
&+ \int_{\Omega_f} \tau_T (\boldsymbol{u} - \boldsymbol{u}_m)\cdot\nabla\eta_f \, R_f^T d\Omega \\
&+ \int_{\Omega_f} \tau_\phi (\boldsymbol{u} - \boldsymbol{u}_m)\cdot\nabla\zeta \, R_f^\phi d\Omega \\
&+ \int_{\Omega_f} \kappa_{dc}^T \nabla\eta_f \cdot \nabla T_f d\Omega + \int_{\Omega_f} \kappa_{dc}^\phi \nabla\zeta\cdot\nabla\phi d\Omega
\end{aligned} \tag{16}
$$

where $\boldsymbol{R}_f^M$, R_f^C, R_f^T, and R_f^ϕ are the residuals based on Eq. 2, Eq. 11, Eq. 12, and Eq. 4. τ_f, τ_C, τ_T, and τ_ϕ are the stabilization parameters based on streamline upwind Petrov-Galerkin (SUPG), pressure-stabilizing Petrov-Galerkin (PSPG), and Least Square on Incompressibility constrain (LSIC) [52–54]. Their definitions are given as

$$
\tau_f = \left[\frac{4}{\Delta t^2} + \frac{4|\boldsymbol{u}|^2}{h^2} + C_I\left(\frac{\nu}{h^2}\right)^2\right]^{-\frac{1}{2}} \tag{17}
$$

$$
\tau_C = \frac{h^2}{12\tau_f} \tag{18}
$$

$$
\tau_T = \left[\frac{4}{\Delta t^2} + \frac{4|\boldsymbol{u}|^2}{h^2} + C_I\left(\frac{\alpha}{h^2}\right)^2\right]^{-\frac{1}{2}} \tag{19}
$$

$$
\tau_\phi = \left[\frac{4}{\Delta t^2} + \frac{4|\boldsymbol{u}|^2}{h^2}\right]^{-\frac{1}{2}} \tag{20}
$$

where Δt is the time step, h is the minimum edge length of the tetrahedron element, $\nu = \frac{\mu_f}{\rho_f}$ and $\alpha = \frac{\kappa_f}{\rho_f c_f}$, C_I is a constant number emanating from the element-wise inverse estimate [55], which is set to 16 in this work. It is noteworthy to mention that the stabilized FEM formulation and its variants, such as Arbitrary Lagrangian-Eulerian technique (ALE-VMS) [56–62] and Space-Time (ST-VMS) technique [63–67], have successfully bean employed as large eddy simulation (LES) models in simulating of a wide range of challenging fluid dynamics and fluid-structure interaction problems. These methods show significant advantages when being deployed to flow problems with moving interfaces and boundaries. Several recent validations and applications include environmental flows [68–71], wind energy [59,72–90], tidal energy [88,91–95], cavitation flows [96,97], supersonic flows [98], bio-mechanics [99–104], gas turbine [105–107], and transportation engineering [108–113].

- At last, W^{bc} represents the weak enforcement of the no-slip boundary conditions at the fluid-solid interface. The last line of Eq. 16 corresponds to the residual-based discontinuity capturing terms, with κ_{dc}^T and κ_{dc}^ϕ given as

$$
\kappa_{dc}^T = \frac{h}{2}\frac{|R_f^T|}{|\nabla T_f|} \tag{21}
$$

$$
\kappa_{dc}^\phi = \frac{h}{2}\frac{|R_f^\phi|}{|\nabla\phi|} \tag{22}
$$

It should be noted that discontinuity capturing is not employed for the Navier-Stokes equations in the present work.

$$
\begin{aligned}
W^{bc}\left(\{\boldsymbol{w}, q\}; \{\boldsymbol{u}, p\}\right) &= -\int_{\Gamma_{fs}} \boldsymbol{w}\cdot\boldsymbol{\sigma} d\Gamma \\
&- \int_{\Gamma_{fs}} \boldsymbol{n}_f \cdot (\nabla^S \boldsymbol{w} + q\boldsymbol{I})\cdot(\boldsymbol{u} - \boldsymbol{u}_g) d\Gamma \\
&- \int_{\Gamma_{fs}^-} \rho_f [\boldsymbol{n}_f\cdot(\boldsymbol{u} - \boldsymbol{u}_m)][\boldsymbol{w}\cdot(\boldsymbol{u} - \boldsymbol{u}_g)] d\Gamma \\
&+ \int_{\Gamma_{fs}} \tau_B \boldsymbol{w}\cdot(\boldsymbol{u} - \boldsymbol{u}_g) d\Gamma
\end{aligned} \tag{23}
$$

where $\boldsymbol{\Gamma}_{fs}^-$ is the inflow portion of $\boldsymbol{\Gamma}_{fs}$, where $\boldsymbol{u}\cdot\boldsymbol{n}_f < 0$. The above weak BC technique can be derived by an augmented Lagrangian approach. The detailed interpretation of each term can be found in [51]. The parameter τ_B is a penalty-like parameter that helps to satisfy the essential BC and improve the stability of the variational formulation. More details about the definition of τ_B and several applications can be found in [51,114,115].

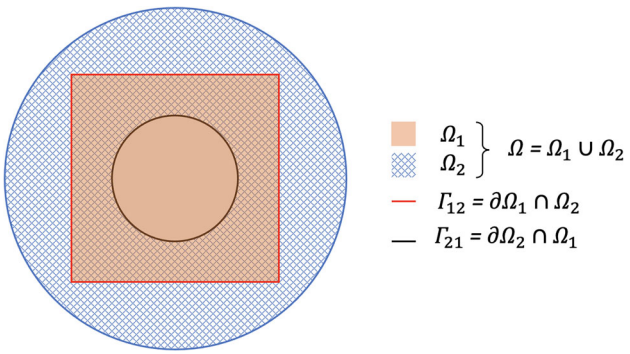

Fig. 2 Overlapping meshes and alternating boundaries

2.3 Overlapping mesh technique and Schwarz alternating method

The variational formulation of Eq. 14 is solved with an overlapping mesh technique enabled by Schwarz alternating method. Schwarz alternating method was first introduced by Hermann Schwarz in the theory of conformal mapping. It has been utilized as an iterative method for solving a problem in the union of two overlapping domains. Without losing generality, let $\mathcal{L}(\boldsymbol{v}) = \boldsymbol{0}$ be a generic problem defined in a domain Ω (a circle). As shown in Fig. 2, the solution of $\mathcal{L}(\boldsymbol{v}) = \boldsymbol{0}$ in Ω is approximated by two overlapping domains, Ω_1 (a rectangle) and Ω_2 (an annulus), with $\partial\Omega_1$ and $\partial\Omega_2$ representing their boundaries. $\Omega = \Omega_1 \cup \Omega_2$. Two non-overlapping boundaries between Ω_1 and Ω_2, which are used to alternate the boundary conditions. They are defined as

$$\Gamma_{12} = \partial\Omega_1 \cap \Omega_2 \tag{24}$$

$$\Gamma_{21} = \partial\Omega_2 \cap \Omega_1 \tag{25}$$

$$\Gamma_{12} \cap \Gamma_{21} = \varnothing \tag{26}$$

Then, the solution of $\mathcal{L}(\boldsymbol{v}) = \boldsymbol{0}$ can be found by the following iterative process.

- **Step 0**: Make an initial guess of $\boldsymbol{v}$ on Γ_{12}
- **Step 1**: Solve $\mathcal{L}(\boldsymbol{v}) = \boldsymbol{0}$ in Ω_1 using the BC on Γ_{12}.
- **Step 2**: Use the solution from **Step 1** to get the BC on Γ_{21}
- **Step 3**: Solve $\mathcal{L}(\boldsymbol{v}) = \boldsymbol{0}$ in Ω_2 using the boundary conditions on Γ_{21}.
- **Step 4**: Use the solution from **Step 3** to get the BC on Γ_{12}, then go to **Step 1**.

2.4 Quasi-direct coupling and time integration

In this section, we deploy the quasi-direct coupling strategy and time integration using the generalized-α time integration scheme in the context of overlapping mesh technique and Schwarz alternating method. We solve the multi-phase convective CHT problem using two overlapping meshes Ω_1 and Ω_2. Ω_1 contains the entire solid sub-domain and partial fluid sub-domain, and Ω_2 occupies the rest fluid sub-domain. Boundary-fitted mesh is utilized to represent the fluid-solid interface. The equations in Ω_1 are solved in a monolithic fashion to satisfy the temperature and flux compatibility constraints automatically. A quasi-direct coupling strategy, similar to those used in fluid-structure interaction analysis [46], is developed to iterate the coupling between Ω_1 and Ω_2.

Without losing generality, let $\{\boldsymbol{R}^M_{f1}, \boldsymbol{R}^C_{f1}, \boldsymbol{R}^\phi_{f1}, \boldsymbol{R}^T_{f1}, \boldsymbol{R}^T_s\}$ denote the generic nodal residuals of fluid momentum, continuity, VoF, fluid temperature, and solid temperature equations in Ω_1 after spatial discretization and $\{\boldsymbol{U}_{f1}, \boldsymbol{P}_{f1}, \boldsymbol{\Phi}_{f1}, \boldsymbol{T}_{f1}, \boldsymbol{T}_s\}$ denote the corresponding unknown nodal vectors for fluid velocity, pressure, VoF, fluid temperature, and solid temperature. In Ω_2, $\{\boldsymbol{R}^M_{f2}, \boldsymbol{R}^C_{f2}, \boldsymbol{R}^\phi_{f2}, \boldsymbol{R}^T_{f2}\}$ denote the generic nodal residuals of momentum, continuity, VoF, and fluid temperature, and $\{\boldsymbol{U}_{f2}, \boldsymbol{P}_{f2}, \boldsymbol{\Phi}_{f2}, \boldsymbol{T}_{f2}\}$ denote the corresponding unknown nodal vectors for fluid velocity, pressure, VoF, and fluid temperature.

Application of the generalized-α time integration scheme to the multi-phase convective CHT variational formulation defined in two overlapping meshes (Ω_1 and Ω_2) leads to two coupled nonlinear systems that need to be solved at every time step, namely: Given the solutions at t_n, find $\{\boldsymbol{U}_{f1}, \boldsymbol{P}_{f1}, \boldsymbol{\Phi}_{f1}, \boldsymbol{T}_{f1}, \boldsymbol{T}_s\}$, $\{\boldsymbol{U}_{f2}, \boldsymbol{P}_{f2}, \boldsymbol{\Phi}_{f2}, \boldsymbol{T}_{f2}\}$, and their time derivatives at t_{n+1}, such that,

$$\begin{Bmatrix} \tilde{\boldsymbol{R}}^M_{f1} \\ \tilde{\boldsymbol{R}}^C_{f1} \\ \tilde{\boldsymbol{R}}^\phi_{f1} \\ \tilde{\boldsymbol{R}}^T_{f1} \\ \tilde{\boldsymbol{R}}^T_s \end{Bmatrix} = \begin{Bmatrix} \boldsymbol{R}^M_{f1} \\ \boldsymbol{R}^C_{f1} \\ \boldsymbol{R}^\phi_{f1} \\ \boldsymbol{R}^T_{f1} \\ \boldsymbol{R}^T_s \end{Bmatrix}_{\left(\dot{\boldsymbol{U}}^{n+\alpha_m}_{f1}, \boldsymbol{U}^{n+\alpha_f}_{f1}, \dot{\boldsymbol{P}}^{n+\alpha_m}_{f1}, \boldsymbol{P}^{n+\alpha_f}_{f1}, \dot{\boldsymbol{\Phi}}^{n+\alpha_m}_{f1}, \boldsymbol{\Phi}^{n+\alpha_f}_{f1}, \dot{\boldsymbol{T}}^{n+\alpha_m}_{f1}, \boldsymbol{T}^{n+\alpha_f}_{f1}, \dot{\boldsymbol{T}}^{n+\alpha_m}_{s}, \boldsymbol{T}^{n+\alpha_f}_{s}\right)} = \boldsymbol{0} \text{ in } \Omega_1 \tag{27}$$

and

$$\begin{Bmatrix} \tilde{\boldsymbol{R}}^M_{f2} \\ \tilde{\boldsymbol{R}}^C_{f2} \\ \tilde{\boldsymbol{R}}^\phi_{f2} \\ \tilde{\boldsymbol{R}}^T_{f2} \end{Bmatrix} = \begin{Bmatrix} \boldsymbol{R}^M_{f2} \\ \boldsymbol{R}^C_{f2} \\ \boldsymbol{R}^\phi_{f2} \\ \boldsymbol{R}^T_{f2} \end{Bmatrix}_{\left(\dot{\boldsymbol{U}}^{n+\alpha_m}_{f2}, \boldsymbol{U}^{n+\alpha_f}_{f2}, \dot{\boldsymbol{P}}^{n+\alpha_m}_{f2}, \boldsymbol{P}^{n+\alpha_f}_{f2}, \dot{\boldsymbol{\Phi}}^{n+\alpha_m}_{f2}, \boldsymbol{\Phi}^{n+\alpha_f}_{f2}, \dot{\boldsymbol{T}}^{n+\alpha_m}_{f2}, \boldsymbol{T}^{n+\alpha_f}_{f2}\right)} = \boldsymbol{0} \text{ in } \Omega_2 \tag{28}$$

where the residuals are enforced to be $\mathbf{0}$ at the intermediate states. The intermediate state of $\boldsymbol{X}$ ($\boldsymbol{X}$ can be $\boldsymbol{U}_{f1}, \boldsymbol{P}_{f1}, \boldsymbol{\Phi}_{f1}, \boldsymbol{T}_{f1}, \boldsymbol{T}_s, \boldsymbol{U}_{f2}, \boldsymbol{\Phi}_{f2}$, or $\boldsymbol{T}_{f2}$) and its time derivative are evaluated as

$$\boldsymbol{X}^{n+\alpha_f} = \alpha_f \boldsymbol{X}^{n+1} + (1-\alpha_f)\boldsymbol{X}^n \tag{29}$$

$$\dot{\boldsymbol{X}}^{n+\alpha_m} = \alpha_m \dot{\boldsymbol{X}}^{n+1} + (1-\alpha_m)\dot{\boldsymbol{X}}^n \tag{30}$$

To link a variable and its time derivative from t_n to t_{n+1}, the Newmark-β scheme is utilized, namely,

$$\boldsymbol{X}^{\alpha} = \boldsymbol{X}^n + \Delta t[\gamma \dot{\boldsymbol{X}}^{\alpha} + (1-\gamma)\dot{\boldsymbol{X}}^n] \tag{31}$$

We adopt the Newton-Raphson method to linearize the nodal nonlinear equations defined in Eq. 27 and Eq. 28 with respect to time derivative at $n+1$ state, which results in a multiple predictor-corrector iterative algorithm. The iteration starts with an initial guess based on the solutions at t_n from both Ω_1 and Ω_2. Then, at l^{th} iteration, the following quasi-direct coupling strategy is employed to solve the systems (Eq. 27 and Eq. 28) defined in Ω_1 and Ω_2. With the above definitions, the following iterative process is repeated until convergence is achieved in both Ω_1 and Ω_2.

- **Step 1:** Use the intermediate states to assemble the residuals and the corresponding Jacobian matrix of the linear system at the lth iteration in Ω_1, namely,

$$\begin{bmatrix}
\frac{\partial \tilde{\boldsymbol{R}}^M_{f1}}{\partial \dot{\boldsymbol{U}}_{f1}} & \frac{\partial \tilde{\boldsymbol{R}}^M_{f1}}{\partial \boldsymbol{P}_{f1}} & \frac{\partial \tilde{\boldsymbol{R}}^M_{f1}}{\partial \dot{\boldsymbol{\Phi}}_{f1}} & \frac{\partial \tilde{\boldsymbol{R}}^M_{f1}}{\partial \dot{\boldsymbol{T}}_{f1}} & \frac{\partial \tilde{\boldsymbol{R}}^M_{f1}}{\partial \dot{\boldsymbol{T}}_{s}} \\
\frac{\partial \tilde{\boldsymbol{R}}^C_{f1}}{\partial \dot{\boldsymbol{U}}_{f1}} & \frac{\partial \tilde{\boldsymbol{R}}^C_{f1}}{\partial \boldsymbol{P}_{f1}} & \frac{\partial \tilde{\boldsymbol{R}}^C_{f1}}{\partial \dot{\boldsymbol{\Phi}}_{f1}} & \frac{\partial \tilde{\boldsymbol{R}}^C_{f1}}{\partial \dot{\boldsymbol{T}}_{f1}} & \frac{\partial \tilde{\boldsymbol{R}}^C_{f1}}{\partial \dot{\boldsymbol{T}}_{s}} \\
\frac{\partial \tilde{\boldsymbol{R}}^\phi_{f1}}{\partial \dot{\boldsymbol{U}}_{f1}} & \frac{\partial \tilde{\boldsymbol{R}}^\phi_{f1}}{\partial \boldsymbol{P}_{f1}} & \frac{\partial \tilde{\boldsymbol{R}}^\phi_{f1}}{\partial \dot{\boldsymbol{\Phi}}_{f1}} & \frac{\partial \tilde{\boldsymbol{R}}^\phi_{f1}}{\partial \dot{\boldsymbol{T}}_{f1}} & \frac{\partial \tilde{\boldsymbol{R}}^\phi_{f1}}{\partial \dot{\boldsymbol{T}}_{s}} \\
\frac{\partial \tilde{\boldsymbol{R}}^T_{f1}}{\partial \dot{\boldsymbol{U}}_{f1}} & \frac{\partial \tilde{\boldsymbol{R}}^T_{f1}}{\partial \boldsymbol{P}_{f1}} & \frac{\partial \tilde{\boldsymbol{R}}^T_{f1}}{\partial \dot{\boldsymbol{\Phi}}_{f1}} & \frac{\partial \tilde{\boldsymbol{R}}^T_{f1}}{\partial \dot{\boldsymbol{T}}_{f1}} & \frac{\partial \tilde{\boldsymbol{R}}^T_{f1}}{\partial \dot{\boldsymbol{T}}_{s}} \\
\frac{\partial \tilde{\boldsymbol{R}}^T_{s}}{\partial \dot{\boldsymbol{U}}_{f1}} & \frac{\partial \tilde{\boldsymbol{R}}^T_{s}}{\partial \boldsymbol{P}_{f1}} & \frac{\partial \tilde{\boldsymbol{R}}^T_{s}}{\partial \dot{\boldsymbol{\Phi}}_{f1}} & \frac{\partial \tilde{\boldsymbol{R}}^T_{s}}{\partial \dot{\boldsymbol{T}}_{f1}} & \frac{\partial \tilde{\boldsymbol{R}}^T_{s}}{\partial \dot{\boldsymbol{T}}_{s}}
\end{bmatrix}^l_{n+1}
\begin{Bmatrix}
\Delta \dot{\boldsymbol{U}}_{f1} \\ \Delta \boldsymbol{P}_{f1} \\ \Delta \dot{\boldsymbol{\Phi}}_{f1} \\ \Delta \dot{\boldsymbol{T}}_{f1} \\ \Delta \dot{\boldsymbol{T}}_{s}
\end{Bmatrix}^l_{n+1}
= -\begin{Bmatrix}
\tilde{\boldsymbol{R}}^M_{f1} \\ \tilde{\boldsymbol{R}}^C_{f1} \\ \tilde{\boldsymbol{R}}^\phi_{f1} \\ \tilde{\boldsymbol{R}}^T_{f1} \\ \tilde{\boldsymbol{R}}^T_{s}
\end{Bmatrix}^l \tag{32}$$

- **Step 2:** Solve the above system and update the solution in Ω_1 based on the following two equations.

$$\begin{Bmatrix}
\dot{\boldsymbol{U}}_{f1} \\ \boldsymbol{P}_{f1} \\ \dot{\boldsymbol{\Phi}}_{f1} \\ \dot{\boldsymbol{T}}_{f1} \\ \dot{\boldsymbol{T}}_{s}
\end{Bmatrix}^{l+1}_{n+1}
= \begin{Bmatrix}
\dot{\boldsymbol{U}}_{f1} \\ \boldsymbol{P}_{f1} \\ \dot{\boldsymbol{\Phi}}_{f1} \\ \dot{\boldsymbol{T}}_{f1} \\ \dot{\boldsymbol{T}}_{s}
\end{Bmatrix}^{l}_{n+1}
+ \begin{Bmatrix}
\Delta \dot{\boldsymbol{U}}_{f1} \\ \Delta \boldsymbol{P}_{f1} \\ \Delta \dot{\boldsymbol{\Phi}}_{f1} \\ \Delta \dot{\boldsymbol{T}}_{f1} \\ \Delta \dot{\boldsymbol{T}}_{s}
\end{Bmatrix}^{l}_{n+1} \tag{33}$$

and

$$\begin{Bmatrix}
\boldsymbol{U}_{f1} \\ \boldsymbol{\Phi}_{f1} \\ \boldsymbol{T}_{f1} \\ \boldsymbol{T}_{s}
\end{Bmatrix}^{l+1}_{n+1}
= \begin{Bmatrix}
\boldsymbol{U}_{f1} \\ \boldsymbol{\Phi}_{f1} \\ \boldsymbol{T}_{f1} \\ \boldsymbol{T}_{s}
\end{Bmatrix}^{l}_{n+1}
+ \Delta t\gamma \begin{Bmatrix}
\Delta \dot{\boldsymbol{U}}_{f1} \\ \Delta \dot{\boldsymbol{\Phi}}_{f1} \\ \Delta \dot{\boldsymbol{T}}_{f1} \\ \Delta \dot{\boldsymbol{T}}_{s}
\end{Bmatrix}^{l}_{n+1} \tag{34}$$

- **Step 3:** Use the updated solutions in Ω_1 to obtain the boundary conditions on Γ_{21} and use the intermediate states to assemble the residuals and the corresponding Jacobian matrix of the linear system at the lth iteration in Ω_2, namely,

$$\begin{bmatrix}
\frac{\partial \tilde{\boldsymbol{R}}^M_{f2}}{\partial \dot{\boldsymbol{U}}_{f2}} & \frac{\partial \tilde{\boldsymbol{R}}^M_{f2}}{\partial \boldsymbol{P}_{f2}} & \frac{\partial \tilde{\boldsymbol{R}}^M_{f2}}{\partial \dot{\boldsymbol{\Phi}}_{f2}} & \frac{\partial \tilde{\boldsymbol{R}}^M_{f2}}{\partial \dot{\boldsymbol{T}}_{f2}} \\
\frac{\partial \tilde{\boldsymbol{R}}^C_{f2}}{\partial \dot{\boldsymbol{U}}_{f2}} & \frac{\partial \tilde{\boldsymbol{R}}^C_{f2}}{\partial \boldsymbol{P}_{f2}} & \frac{\partial \tilde{\boldsymbol{R}}^C_{f2}}{\partial \dot{\boldsymbol{\Phi}}_{f2}} & \frac{\partial \tilde{\boldsymbol{R}}^C_{f2}}{\partial \dot{\boldsymbol{T}}_{f_{f2}}} \\
\frac{\partial \tilde{\boldsymbol{R}}^\phi_{f2}}{\partial \dot{\boldsymbol{U}}_{f2}} & \frac{\partial \tilde{\boldsymbol{R}}^\phi_{f2}}{\partial \boldsymbol{P}_{f2}} & \frac{\partial \tilde{\boldsymbol{R}}^\phi_{f2}}{\partial \dot{\boldsymbol{\Phi}}_{f2}} & \frac{\partial \tilde{\boldsymbol{R}}^\phi_{f2}}{\partial \dot{\boldsymbol{T}}_{f2}} \\
\frac{\partial \tilde{\boldsymbol{R}}^T_{f2}}{\partial \dot{\boldsymbol{U}}_{f2}} & \frac{\partial \tilde{\boldsymbol{R}}^T_{f2}}{\partial \boldsymbol{P}_{f2}} & \frac{\partial \tilde{\boldsymbol{R}}^T_{f2}}{\partial \dot{\boldsymbol{\Phi}}_{f2}} & \frac{\partial \tilde{\boldsymbol{R}}^M_{f2}}{\partial \dot{\boldsymbol{T}}_{f2}}
\end{bmatrix}^l_{n+1}
\begin{Bmatrix}
\Delta \dot{\boldsymbol{U}}_{f2} \\ \Delta \boldsymbol{P}_{f2} \\ \Delta \dot{\boldsymbol{\Phi}}_{f2} \\ \Delta \dot{\boldsymbol{T}}_{f2}
\end{Bmatrix}^l_{n+1}
= -\begin{Bmatrix}
\tilde{\boldsymbol{R}}^M_{f2} \\ \tilde{\boldsymbol{R}}^C_{f2} \\ \tilde{\boldsymbol{R}}^\phi_{f2} \\ \tilde{\boldsymbol{R}}^T_{f2}
\end{Bmatrix}^l \tag{35}$$

- **Step 4:** Solve the above linear system and update the solutions in Ω_2 based on

$$\begin{Bmatrix}
\dot{\boldsymbol{U}}_{f2} \\ \boldsymbol{P}_{f2} \\ \dot{\boldsymbol{\Phi}}_{f2} \\ \dot{\boldsymbol{T}}_{f2}
\end{Bmatrix}^{l+1}_{n+1}
= \begin{Bmatrix}
\dot{\boldsymbol{U}}_{f2} \\ \boldsymbol{P}_{f2} \\ \dot{\boldsymbol{\Phi}}_{f2} \\ \dot{\boldsymbol{T}}_{f2}
\end{Bmatrix}^{l}_{n+1}
+ \begin{Bmatrix}
\Delta \dot{\boldsymbol{U}}_{f2} \\ \Delta \boldsymbol{P}_{f2} \\ \Delta \dot{\boldsymbol{\Phi}}_{f2} \\ \Delta \dot{\boldsymbol{T}}_{f2}
\end{Bmatrix}^{l}_{n+1} \tag{36}$$

and

$$\begin{Bmatrix}
\boldsymbol{U}_{f2} \\ \boldsymbol{\Phi}_{f2} \\ \boldsymbol{T}_{f2}
\end{Bmatrix}^{l+1}_{n+1}
= \begin{Bmatrix}
\boldsymbol{U}_{f2} \\ \boldsymbol{\Phi}_{f2} \\ \boldsymbol{T}_{f2}
\end{Bmatrix}^{l}_{n+1}
+ \Delta t\gamma \begin{Bmatrix}
\Delta \dot{\boldsymbol{U}}_{f2} \\ \Delta \dot{\boldsymbol{\Phi}}_{f2} \\ \Delta \dot{\boldsymbol{T}}_{f2}
\end{Bmatrix}^{l}_{n+1} \tag{37}$$

- **Step 5:** Use the above updated solutions in Ω_2 to obtain the boundary conditions on Γ_{12}. Then, go to **Step 1**

Remark 1 The linear systems defined in Eq. 32 and Eq. 35 are solved by a generalized minimal residual method (GMRES) with a three-level recursive preconditioning technique, proposed in [116].

Remark 2 One should note that pressure field at $n+1$, rather than α state, is used to evaluate the residuals (Eq. 27 and Eq. 28). A discussion on this choice and its significance can be found in [117].

Remark 3 In **Step 3** and **Step 5**, both essential and natural BCs can be alternated between Ω_1 and Ω_2. The prescribed values of each node on Γ_{12} (or Γ_{21}) can be obtained by interpolation using the shape functions of the element in Ω_2 (or Ω_1), which contains this node. For pure stationary overlapping meshes, the point-to-element location process is pre-computed to save computational cost. For moving overlapping meshes, an octree-based algorithm [35,116] is adopted to speed up the search process.

3 Numerical Examples

We present numerical examples to demonstrate the proposed framework's accuracy and flexibility in handling moving objects and apply the framework to simulate realistic water quenching processes of metallic structures.

3.1 Poisson equation

We first solve a one-dimensional Poisson equation using the overlapping framework. Poisson equation has wide applications in electromagnetic mechanics, static heat conduction, and even porous media flow problems. This example is to study the accuracy and convergence rate of the proposed method. The problem is defined as,

$$\nabla^2 u = (x+2)e^x \quad x \in [-1, 1] \tag{38}$$

$$u(-1) = -\frac{1}{e} \tag{39}$$

$$u(1) = e \tag{40}$$

where $u = u(x)$ is the unknown solution. This boundary value problem has the following exact solution.

$$u = xe^x \tag{41}$$

We perform refinement study of this problem. The overlapping decomposition of the domain consists of two parts as shown in Fig. 3. One part is defined in $\{x| -1 \leq x \leq 0.25\}$, and the other is defined in $\{x| -0.25 \leq x \leq 1\}$. Four meshes with uniform element sizes ($h = 1.25/100, 1.25/200, 1.25/400, 1.25/800$) are tested.

Figure 4 shows the solution from the coarsest mesh ($h = 1.25/100$). **Mesh 1** and **Mesh 2** deliver almost the identical solution in the overlapped region.

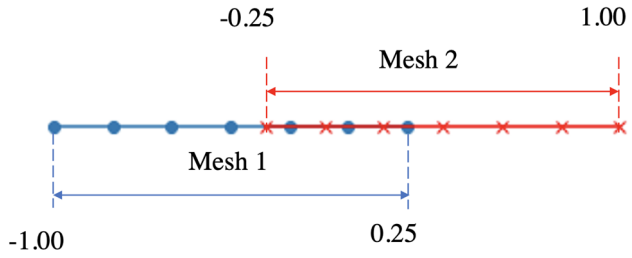

Fig. 3 Two overlapping meshes used to solve the Poisson equation

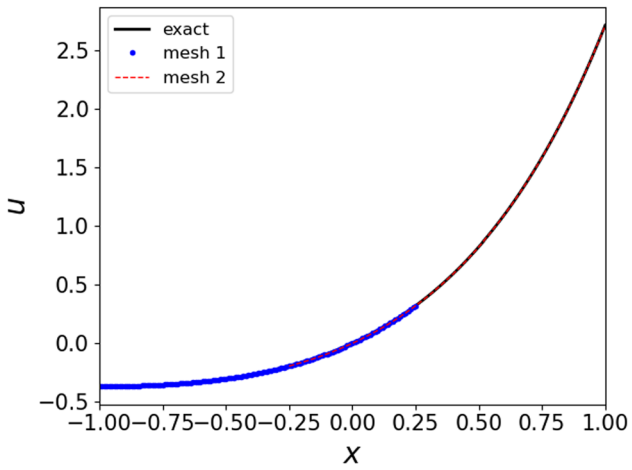

Fig. 4 Comparison between the exact solution and the numerical prediction with $h = 1.25/100$

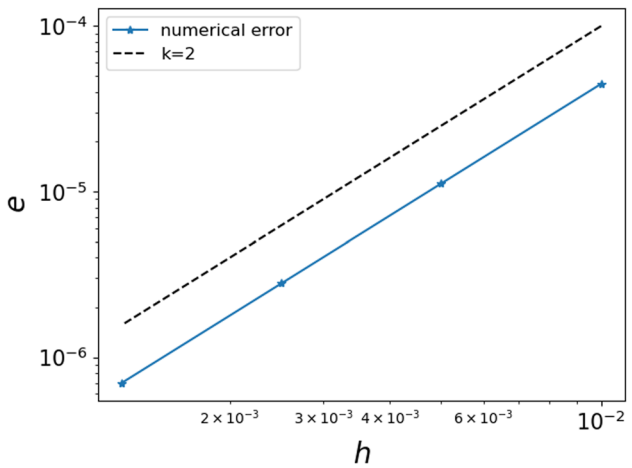

Fig. 5 L_2 norm of error with different resolutions $h = 1.25/100, 1.25/200, 1.25/400$, and $1.25/800$. The black dashed line is a reference line with slope 2

The L_2 norm of the error with different mesh sizes is plotted in Fig. 5, showing that the error reduces with mesh refinement with a convergence rate of around 2.00.

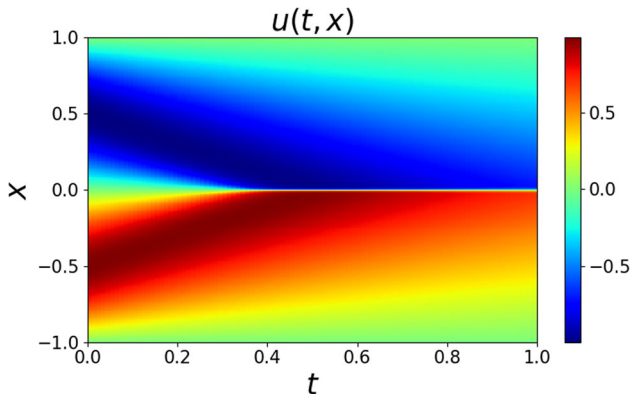

Fig. 6 Spatio-temporal solution contour of a Burger's equation using $h = 1/200$

Table 1 Properties of the quenching medium and the AL part

Property	Notation	Value
Water density	ρ_l	1000 kg/m^3
Water heat capacity	c_l	4200 J/(kg · K)
Water heat conductivity	κ_l	0.65 W/(m · K)
Water viscosity	μ_l	10^{-3}Pa · s
Vapor density	ρ_v	1.23 kg/m^3
Vapor heat capacity	c_v	1996 J/(kg · K)
Vapor heat conductivity	κ_v	0.067 W/(m · K)
Vapor viscosity	μ_v	1.3×10^{-4} Pa · s
Part density	ρ_s	2700 kg/m^3
Part heat capacity	c_s	921.0 J/(kg · K)
Part heat conductivity	κ_s	205.0 W/(m · K)
Latent heat of vaporization	L	2.265×10^6J/kg

3.2 Burgers' equation

We continue to solve a one-dimensional Burgers' equation. The Burgers' equation can be viewed as a Navier-Stokes momentum equation without pressure. The Burgers' equation occurs in various areas of applied mathematics and engineering science, such as nonlinear acoustics, gas dynamics, and traffic flow. The study's purpose is to verify whether the overlapping technique using Schwarz alternating method delivers the same result as a single mesh-based approach. The Burger's equation considered in this paper with initial and boundary conditions is defined as

$$\frac{\partial u}{\partial t} + u\frac{\partial u}{\partial x} = \nu\frac{\partial^2 u}{\partial x^2} \quad x \in [-1, 1] \tag{42}$$

$$u(t, -1) = u(t, 1) = 0 \tag{43}$$

$$u(0, x) = sin(-\pi x) \tag{44}$$

where $u = u(t, x)$ is the unknown field and ν is the diffusion coefficient, which is set to $\frac{0.01}{\pi}$ in this paper. The simulation domain is the same as that of the previous section. Four different mesh resolutions with $h = 1.25/50$, $1.25/100$, $1.25/200$, and $1.25/400$ are selected to investigate the problem. Time step Δt is set to 0.01 for all the cases. The contour of solution of $u(t, x)$ based on the mesh with $h = 1.25/200$ is shown in Fig. 6. The solutions of $u(t, x)$ from all the meshes at three different time instances are plotted in Fig. 7, in which a reference result based on a single mesh-based simulation ($h = 1/3200$) is plotted for comparison. The plot shows that the same results are obtained in the overlapped region from both meshes. The comparison with the single mesh-based solution also indicates that all the overlapping meshes deliver accurate predictions and quickly converge to the reference results with mesh refinement.

3.3 Simulation of water quenching process of a stationary metallic part

In this section, we apply the proposed framework to simulate a water quenching process of a stationary aluminum (AL) part. The simulation aims to enable accurate temperature prediction inside the part directly from the quenching parameters without invoking the empirical heat transfer coefficients. This water quenching process was experimentally investigated in [2], which employs a cubic water tank to quench a metallic structure based on AL-319 alloy. The structure is first heated in a furnace up to 500 °C and then immersed into the quenching tank with an initial temperature of 75 °C. No agitation flow is applied during the process. The mechanical and thermal properties of the quenching medium (based on water) and quenched AL part, determined by ThermoCalc®, are listed in Table 1. The computer-aided design (CAD) model of the structure, its dimensions, and the locations of installed thermocouples are shown in Fig. 8. The simulation domain is a box with dimensions 800 mm × 800 mm × 900 mm. The simulation domain is discretized by two overlapping meshes (see Fig. 9), in which a boundary-fitted box mesh (**Mesh1**) with dimensions 120 mm × 200 mm × 300 mm is used to represent the whole solid domain and partial fluid domain. A complementary mesh (Mesh 2) is used for the rest of the fluid domain. The computational domain is meshed by linear tetrahedral elements. A local refinement (with h = 1.5 mm) is designed around the part to better capture the boiling and condensation processes. The total number of nodes and elements of the two meshes employed in the simulation is listed in Table 2. The following boundary conditions are applied. For the fluid field, a no-penetration boundary condition is applied to every surface of the entire computational domain. For the temperature field, a no-flux boundary condition is applied to every surface except the top surface, where a convective boundary condition is applied. Constant Δt = 0.25 ms is used throughout the simulation. To validate the overlapping mesh technique, we conduct a single mesh-based

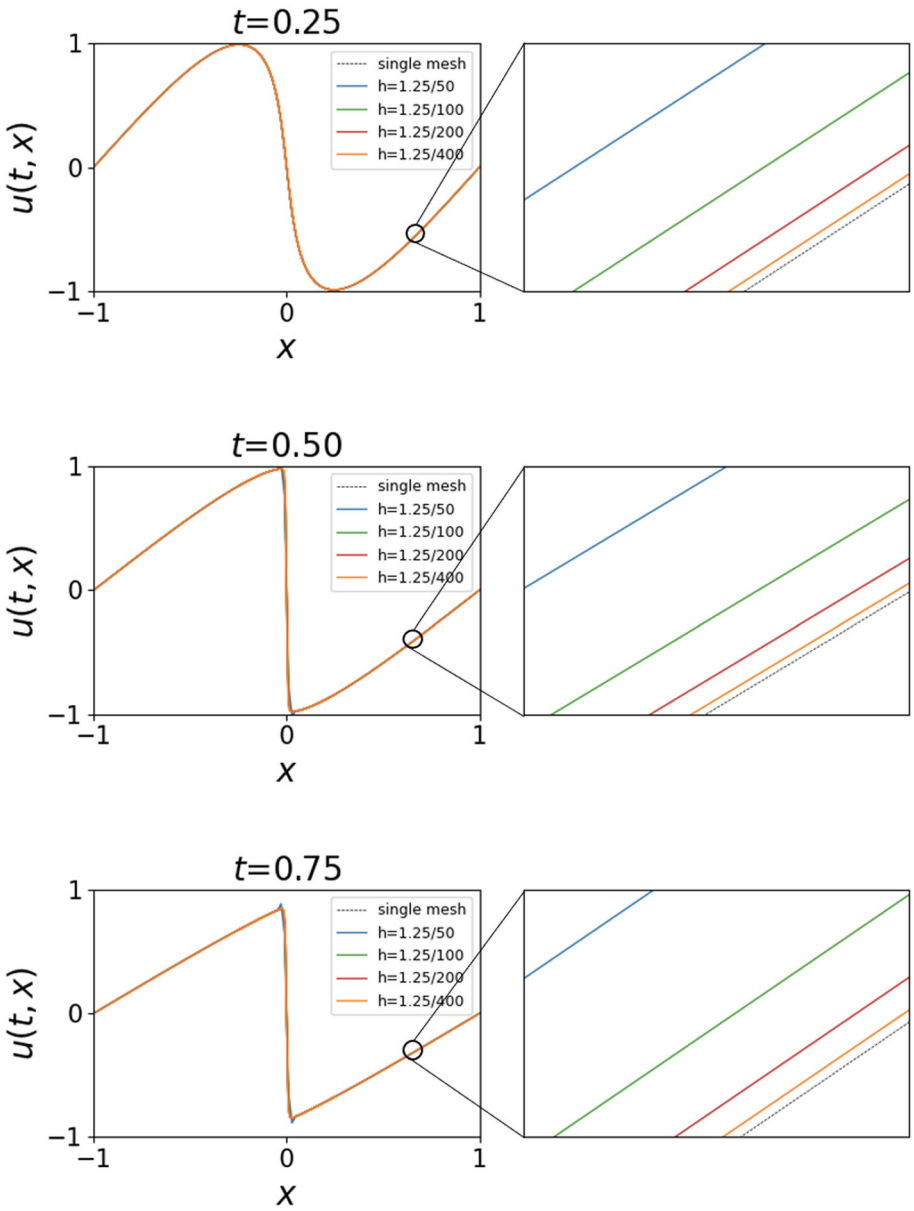

Fig. 7 The solution of Burgers' equation: Overlapping mesh method solutions at t=0.25, 0.50, 0.75 with element length $h = 1.25/50$, $1.25/100$, $1.25/200$, and $1.25/400$; the single mesh result using $h = 1/3200$ is also plotted for comparison (This high resolution is chosen to ensure its credibility as a reference solution)

simulation employing the same setup parameters. Both simulations are performed in parallel using Stampede2 at Texas Advanced Computing Center (TACC) with 192 processors. The simulations run for 10 s in physical time.

Figure 10 shows the vapor plume and temperature in the part at three time instances during the quenching process. In the beginning, a large amount of vapor is generated by the evaporation due to the high part temperature. The vapors rapidly rise towards the top surface due to buoyancy, introducing turbulent multi-phase flows in the tank (see Fig. 11), which results in non-uniform temperature distribution in the part (see Fig. 10 (B)). As the heat is transferred from the part to the quenching medium, the part surface temperature decreases and slows down the vapor generation. Figures 11 and 12 show the comparison between the simulations using

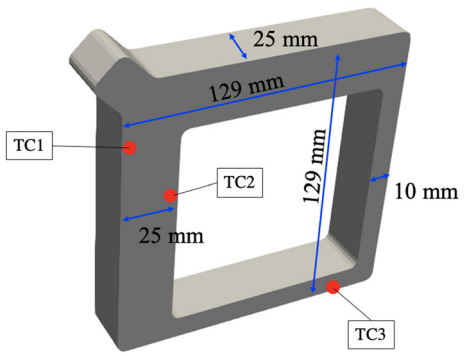

Fig. 8 CAD model of the quenched AL part. The thermocouples are placed 12.5 mm beneath the surface markers

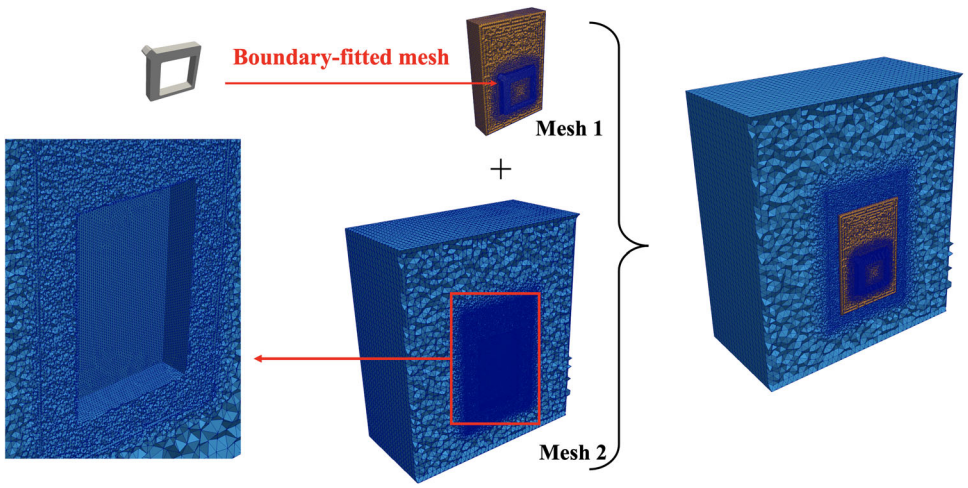

Fig. 9 Overlapping meshes employed in the simulation

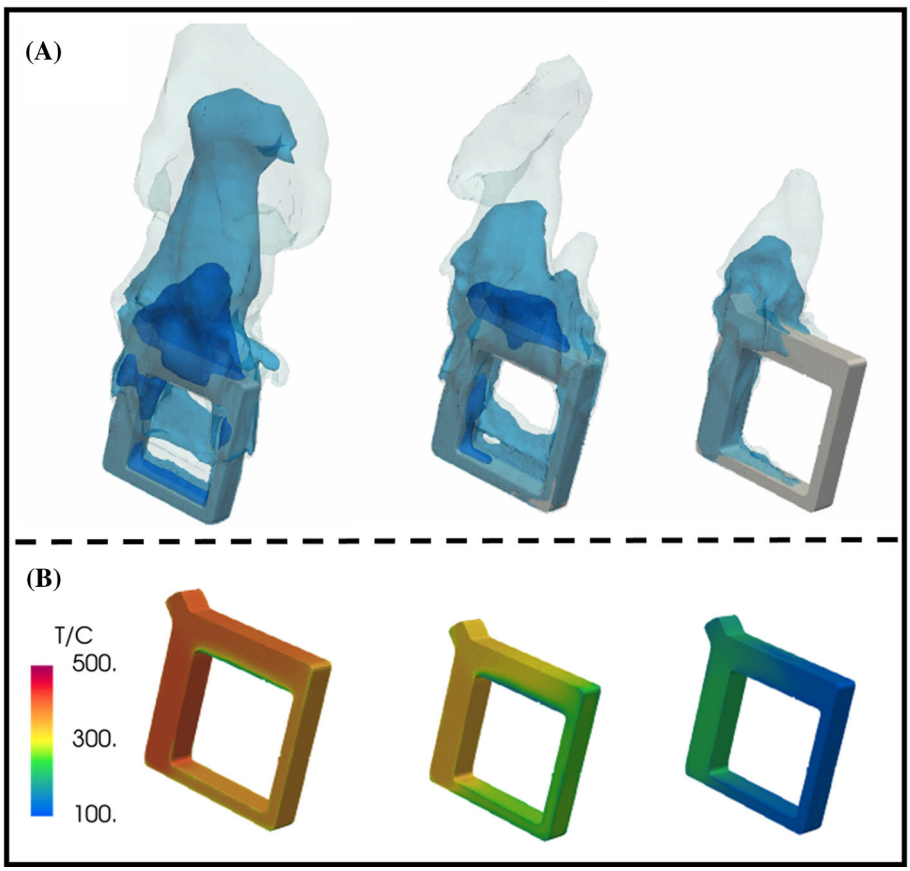

Fig. 10 **(A)** Vapor plume. **(B)** Part temperature

overlapping meshes and a single mesh in the prediction of temperature distribution, vapor fraction, and velocity magnitude on the middle plane of the tank. The overlapping mesh approach can deliver continuous solutions across the overlapping boundaries. Similar predictions of flow and temperature fields are observed between the single mesh and overlapping approaches. At last, we plot the predicted temperature history of the three thermocouples (see Fig. 8 for their locations) in Fig. 13, in which the experimental data obtained from [2] at the same locations are plotted for comparison. The simulated results agree well with the measured data. We can also see that the proposed framework using overlapping meshes provides equivalent accuracy as its single mesh-based counterpart.

Table 2 Number of nodes and elements of the meshes employed in the quenching process of a stationary AL part

	Mesh 1 (Ω_1)	Mesh 2 (Ω_2)
Number of nodes	353,308	829,965
Number of elements	2,069,330	4,788,939

3.4 Simulation of water quenching process of a rotating metallic gear

We further demonstrate the proposed framework's capability in handling moving objects by applying it to simulate a water quenching process of a rotating metallic gear. The mechanical and thermal properties of the quenching medium and the gear are the same as those used in the previous section. The computer-aided design (CAD) model of the gear and its dimensions are depicted in Fig. 14. Figure 15 shows the overlapping meshes employed in the simulations. The entire computational domain is a box with dimensions 480 mm × 480 mm × 350 mm. The computational domain consists of two overlapping meshes. Similar to the previous section, one boundary-fitted cylindrical mesh (**Mesh 1**) with 340 mm in diameter and 120 mm in height is utilized to represent the whole solid domain and partial fluid domain. A complementary mesh (**Mesh 2**) is used to represent the rest fluid domain. The cylindrical mesh rotates with the rotating gear through an ALE technique to maintain boundary-fitted surface representation. A local refinement (with h = 1 mm) is designed around the gear to better capture the boiling and condensation processes. Table 3 summarizes the statistics of the meshes. To investigate the effects of gear rotation on the flow and temperature field, a stationary case and a rotational case with speed $\omega = 4\pi$ rad/s are simulated using the same mesh. Both cases utilize a constant Δt =0.25 ms throughout the simulations. The following boundary conditions are applied on the boundaries of the entire computational domain. For the fluid field, a no-penetration boundary condition is applied to every surface. For the temperature field, a no-flux boundary condition is applied to every surface except the top surface, where a convective boundary condition is applied. The simulations are performed in the same parallel environment in Stampede2 of TACC as specified in the previous section.

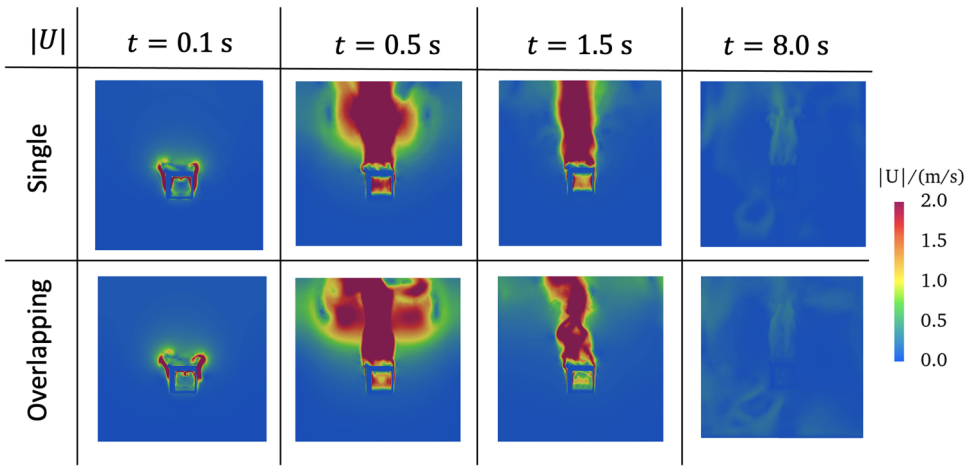

Fig. 11 Comparison of velocity prediction between single mesh and overlapping mesh approaches: t = 0.1 s, 0.5 s, 1.5 s, and 8.0 s

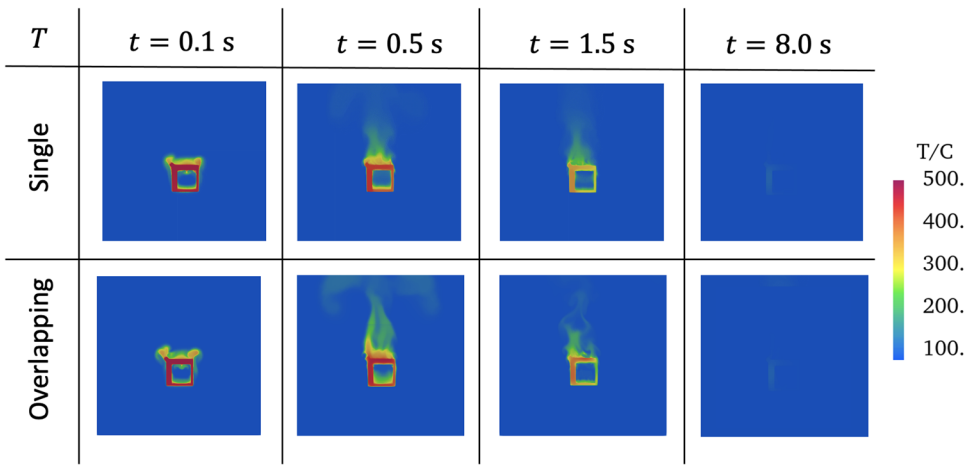

Fig. 12 Comparison of temperature prediction between single mesh and overlapping mesh approaches: t = 0.1 s, 0.5 s, 1.5 s, and 8.0 s

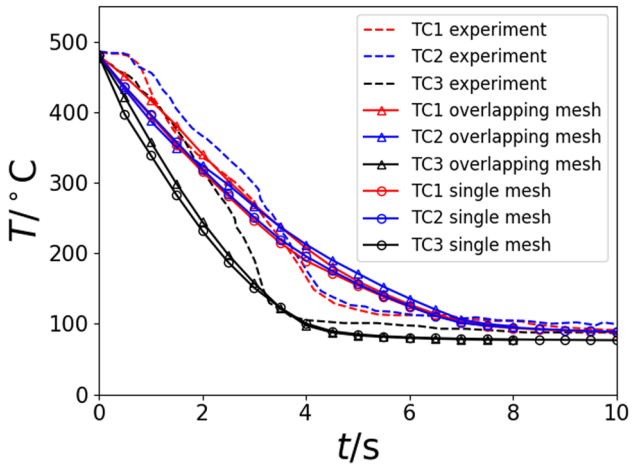

Fig. 13 Temperature history on three thermocouples: experimental measurement vs. numerical predictions using single mesh and overlapping mesh approaches

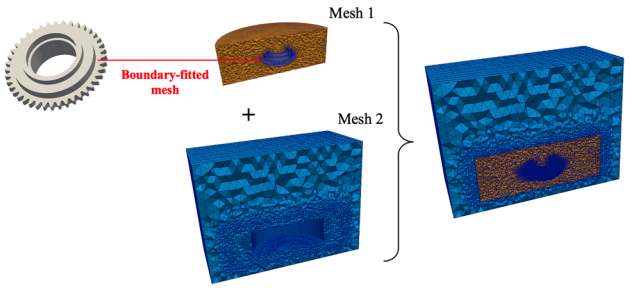

Fig. 15 Overlapping meshes employed in the water processes of a metallic gear

Table 3 Number of nodes and elements of the meshes in the gear quenching case

	Mesh 1 (Ω_1)	Mesh 2 (Ω_2)
Number of nodes	473,949	371,135
Number of elements	2,770,121	2,148,150

Comparisons between the rotational case and the stationary case are shown in Figs. 16 and 17. Figure 16 plots the velocity magnitude and vapor fraction on a horizontal plane of the computational domain at $t = 1$ s. The motion of the gear results in a more substantial flow motion in the tank and facilitates the traveling of vapors from the gear surface to the interior of the tank. Figure 17 shows the vapor iso-surfaces and temperature contours on the gear surface at $t = 1$ s. Distinctive vapor plume profiles are observed between the two cases. The traces of the rotation of the gear can be found in the temperature contour on the gear surface. At last, the temperature history at five representative locations in the gear's cross-section (averaged over all the gear teeth) is plotted in Fig. 18. In general, the motion of the gear speeds up the cooling process. The effect becomes more pronounced in TC2, which is closest to the gear's tip that has the biggest linear speed among these locations.

4 Conclusions

In this paper, we presented a new computational framework for the multi-phase convective conjugate heat transfer systems arising from heat treatment and composite manufacturing processes. The paper tried to address some of the longstanding challenges of existing boundary-fitted and immersed boundary approaches in handling this class of problems stemming from heat flux enforcement, mesh flexibility and boundary layer resolution. The novelty of the proposed framework is marked by the meticulous integration of an overlapping mesh technique, stabilized methods for thermal multi-phase flows, and a novel quasi-direct coupling strategy with Schwarz alternating method. The proposed framework allows highly accurate resolution of the fluid-solid interface and boundary layer behavior and simultaneously offers tremendous mesh flexibility in handling moving structures. We verified and validated the proposed framework through benchmark problems and real-world quenching processes. The simulated results show good agreement with experimental measurements. Through these demonstrations, we believe the proposed framework possesses excellent potential in multi-phase convective CHT systems and can be applied to a wide range of heat treatment and advanced manufacturing processes.

Fig. 14 CAD model of the gear and its dimensions

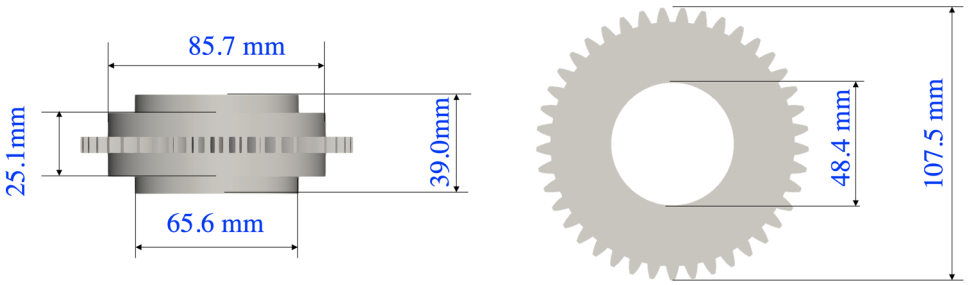

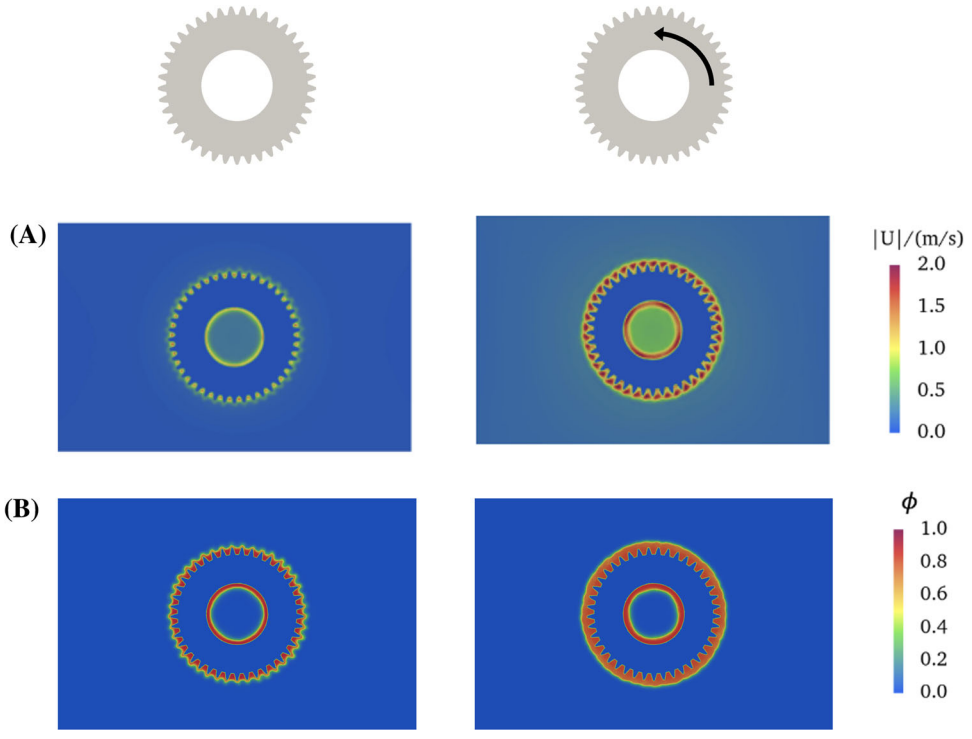

Fig. 16 Comparison between water quenching processes with a stationary gear and a rotational gear. **(A)** Velocity magnitude on a horizontal plane at $t = 1.0$ s. **(B)** Vapor fraction on a horizontal plane at $t = 1.0$ s

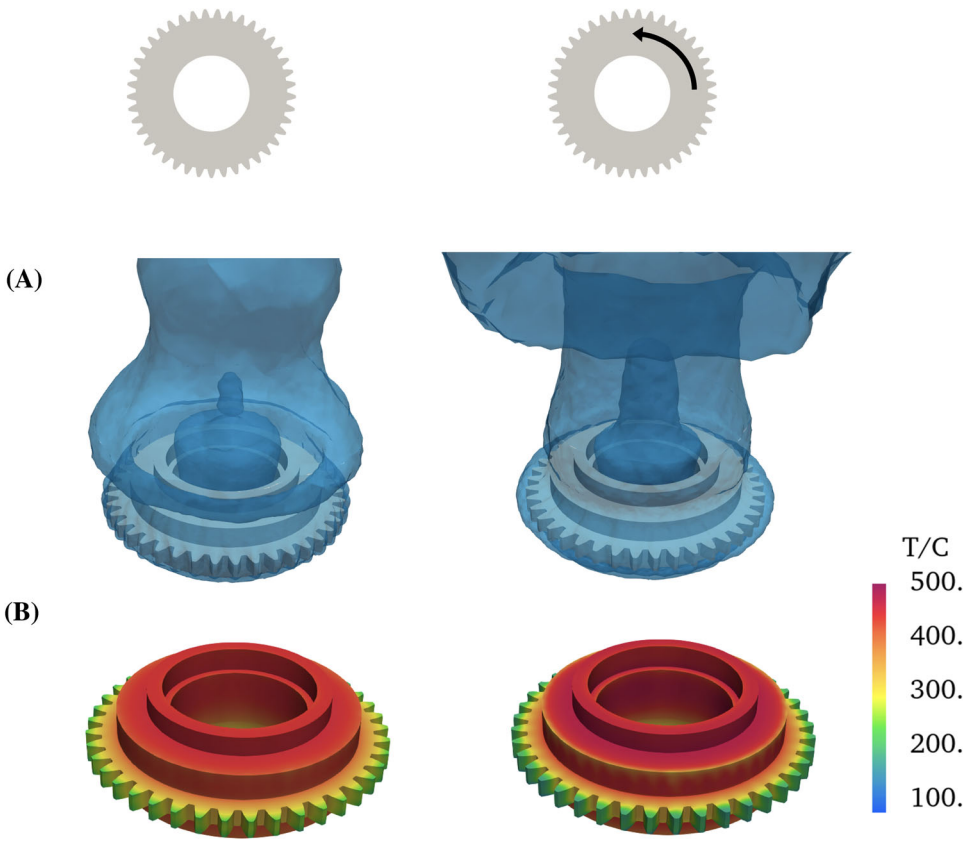

Fig. 17 Comparison between water quenching processes with a stationary gear and a rotational gear. **(A)** Vapor flumes at $t = 1.0$ s. **(B)** Temperature contour on the gear's surface at $t = 1.0$ s

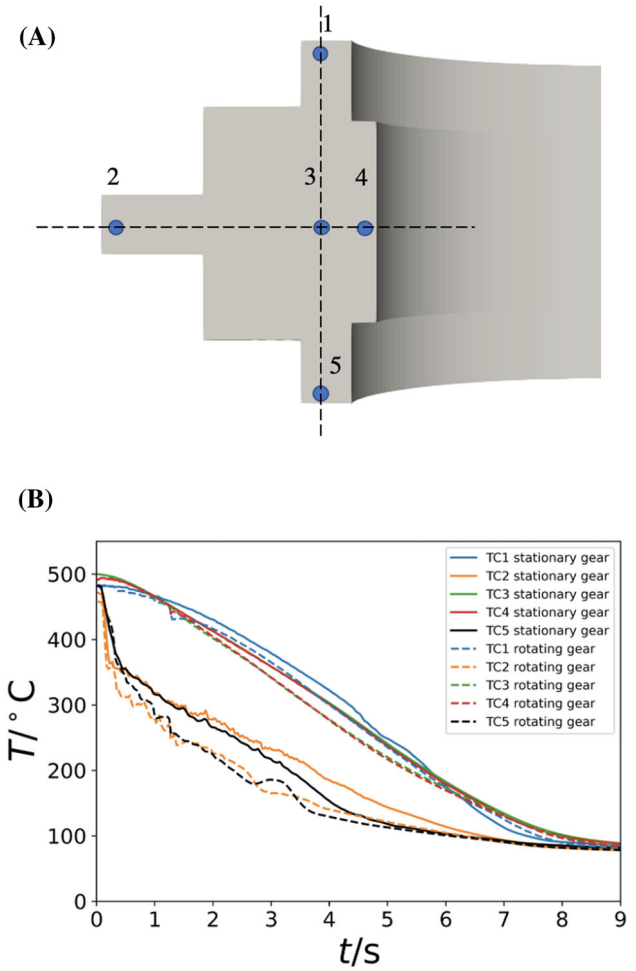

Fig. 18 **(A)** Location of thermocouples. **(B)** Comparison of the time history of temperature of these thermocouples between the stationary and rotational cases

Acknowledgements This work is funded by the U.S. Navy through the contract of N68335-21-C-0057. J. Yan also wants to acknowledge the support of computational facilities from Texas Advanced Computing Center through the allocation of CTS20014.

References

1. Luikov A, Perelman T, Levitin R, Gdalevich L (1970) Heat transfer from a plate in a compressible gas flow. Int J Heat Mass Transf 13(8):1261–1270
2. Xiao B, Wang Q, Jadhav P, Li K (2010) An experimental study of heat transfer in aluminum castings during water quenching. J Mater Process Technol 210(14):2023–2028
3. Lua J, Yan J, Li P, Zhao Z, Karuppiah A, Stuebner M (2021) Novel multi-physics-based modeling of a quenching process with thermal-metallurgical-mechanical interactions in aluminum components, in: 77th Annual Vertical Flight Society Forum and Technology Display: The Future of Vertical Flight, FORUM 2021, Vertical Flight Society
4. Hughes TJR, Liu WK, Zimmermann TK (1981) Lagrangian-Eulerian finite element formulation for incompressible viscous flows. Comput Methods Appl Mech Eng 29:329–349
5. Takizawa K, Bazilevs Y, Tezduyar T (2012) Space-time and ALE-VMS techniques for patient-specific cardiovascular fluid-structure interaction modeling. Archives of Computational Methods in Engineering 19(2):171–225
6. Bazilevs Y, Hsu M, Takizawa K, Tezduyar T (2012) ALE-VMS and ST-VMS methods for computer modeling of wind-turbine rotor aerodynamics and fluid-structure interaction. Math Models Methods Appl Sci 22(supp02):1230002
7. Calderer R, Zhu L, Gibson R, Masud A (2015) Residual-based turbulence models and arbitrary lagrangian-eulerian framework for free surface flows. Math Models Methods Appl Sci 25(12):2287–2317
8. Tezduyar TE, Sathe S, Pausewang J, Schwaab M, Christopher J, Crabtree J (2008) Interface projection techniques for fluid-structure interaction modeling with moving-mesh methods. Comput Mech 43:39–49. https://doi.org/10.1007/s00466-008-0261-7
9. Johnson AA, Tezduyar TE (1994) Mesh update strategies in parallel finite element computations of flow problems with moving boundaries and interfaces. Comput Methods Appl Mech Eng 119:73–94. https://doi.org/10.1016/0045-7825(94)00077-8
10. Hsu M-C, Bazilevs Y (2012) Fluid-structure interaction modeling of wind turbines: simulating the full machine. Comput Mech. https://doi.org/10.1007/s00466-012-0772-0
11. Peskin CS (1972) Flow patterns around heart valves: a numerical method. J Comput Phys 10(2):252–271
12. Parvizian J, Düster A, Rank E (2007) Finite cell method: h- and p- extension for embedded domain methods in solid mechanics. Comput Mech 41:122–133
13. Düster A, Parvizian J, Yang Z, Rank E (2008) The finite cell method for three-dimensional problems of solid mechanics. Comput Methods Appl Mech Eng 197(45–48):3768–3782
14. Xu F, Schillinger D, Kamensky D, Varduhn V, Wang C, Hsu M (2016) The tetrahedral finite cell method for fluids: Immersogeometric analysis of turbulent flow around complex geometries. Computers & Fluids 141:135–154
15. Main A, Scovazzi G (2018) The shifted boundary method for embedded domain computations. part i: Poisson and stokes problems,. J Comput Phys 372:972–995
16. Main A, Scovazzi G (2018) The shifted boundary method for embedded domain computations. part ii: Linear advection–diffusion and incompressible navier–stokes equations,. J Comput Phys 372:996–1026
17. Song T, Main A, Scovazzi G, Ricchiuto M (2018) The shifted boundary method for hyperbolic systems: Embedded domain computations of linear waves and shallow water flows. J Comput Phys 369:45–79
18. Li K, Atallah N, Main A, Scovazzi G (2020) The shifted interface method: A flexible approach to embedded interface computations. Int J Numer Meth Eng 121(3):492–518
19. Colomés O, Main A, Nouveau L, Scovazzi G (2021) A weighted shifted boundary method for free surface flow problems. J Comput Phys 424:109837
20. Hansbo A, Hansbo P (2002) An unfitted finite element method, based on nitsche's method, for elliptic interface problems. Comput Methods Appl Mech Eng 191(47–48):5537–5552
21. Bazilevs Y, Kamran K, Moutsanidis G, Benson DJ, Oñate E (2017) A new formulation for air-blast fluid-structure interaction using an immersed approach. Part I: basic methodology and FEM-based simulations, Computational Mechanics 60(1):83–100
22. Bazilevs Y, Moutsanidis G, Bueno J, Kamran K, Kamensky D, Hillman MC, Gomez H, Chen JS (2017) A new formulation for air-blast fluid-structure interaction using an immersed approach:

Part II–coupling of IGA and meshfree discretizations. Comput Mech 60(1):101–116
23. Behzadinasab M, Moutsanidis G, Trask N, Foster J, Bazilevs Y (2021) Coupling of iga and peridynamics for air-blast fluid-structure interaction using an immersed approach. Forces in Mechanics 4:100045
24. Moutsanidis G, Koester J, Tupek M, Chen J, Bazilevs Y (2020) Treatment of near-incompressibility in meshfree and immersed-particle methods. Computational particle mechanics 7(2):309–327
25. Moutsanidis G, Kamensky D, Chen J, Bazilevs Y (2018) Hyperbolic phase field modeling of brittle fracture: Part ii-immersed iga-rkpm coupling for air-blast-structure interaction. J Mech Phys Solids 121:114–132
26. Liu WK, Liu Y, Farrell D, Zhang L, Wang XS, Fukui Y, Patankar N, Zhang Y, Bajaj C, Lee J et al (2006) Immersed finite element method and its applications to biological systems. Comput Methods Appl Mech Eng 195(13–16):1722–1749
27. Zhang L, Gerstenberger A, Wang X, Liu W (2004) Immersed finite element method. Comput Methods Appl Mech Eng 193(21–22):2051–2067
28. Zhang LT, j. v. n. p. y. p. Gay M Immersed finite element method for fluid-structure interactions
29. Wang X, Zhang L (2010) Interpolation functions in the immersed boundary and finite element methods. Comput Mech 45(4):321–334
30. Wang X, Zhang L, Liu W (2009) On computational issues of immersed finite element methods. J Comput Phys 228(7):2535–2551
31. Wang X, Zhang L (2013) Modified immersed finite element method for fully-coupled fluid-structure interactions. Comput Methods Appl Mech Eng 267:150–169
32. Schillinger D, Dede L, Scott MA, Evans J, Borden M, Rank E, Hughes T (2012) An isogeometric design-through-analysis methodology based on adaptive hierarchical refinement of nurbs, immersed boundary methods, and t-spline cad surfaces. Comput Methods Appl Mech Eng 249:116–150
33. Hsu M-C, Kamensky D, Xu F, Kiendl J, Wang C, Wu MCH, Mineroff J, Reali A, Bazilevs Y, Sacks MS (2015) Dynamic and fluid-structure interaction simulations of bioprosthetic heart valves using parametric design with T-splines and Fung-type material models. Comput Mech 55:1211–1225
34. Kamensky D, Hsu M-C, Schillinger D, Evans JA, Aggarwal A, Bazilevs Y, Sacks MS, Hughes TJR (2015) An immersogeometric variational framework for fluid-structure interaction: Application to bioprosthetic heart valves. Comput Methods Appl Mech Eng 284:1005–1053
35. Zhu Q, Xu F, Xu S, Hsu M, Yan J (2020) An immersogeometric formulation for free-surface flows with application to marine engineering problems. Comput Methods Appl Mech Eng 361:112748
36. Volkov E (1968) The method of composite meshes for finite and infinite regions with piecewise smooth boundary. Trudy Matematicheskogo Instituta imeni VA Steklova 96:117–148
37. Henshaw W (1994) A fourth-order accurate method for the incompressible navier-stokes equations on overlapping grids. J Comput Phys 113(1):13–25
38. Henshaw W, Chand K (2009) A composite grid solver for conjugate heat transfer in fluid-structure systems. J Comput Phys 228(10):3708–3741
39. Appelö D, Banks J, Henshaw W, Schwendeman D (2012) Numerical methods for solid mechanics on overlapping grids: Linear elasticity. J Comput Phys 231(18):6012–6050
40. Koblitz A, Lovett S, Nikiforakis N, Henshaw W (2017) Direct numerical simulation of particulate flows with an overset grid method. J Comput Phys 343:414–431
41. Meng F, Banks J, Henshaw W, Schwendeman D (2020) Fourth-order accurate fractional-step imex schemes for the incompressible navier-stokes equations on moving overlapping grids. Comput Methods Appl Mech Eng 366:113040
42. MEAKIN R (1993) Moving body overset grid methods for complete aircraft tiltrotor simulations, in: 11th Computational Fluid Dynamics Conference, p. 3350
43. Chan W (2009) Overset grid technology development at nasa ames research center. Computers & Fluids 38(3):496–503
44. Chandar D, Damodaran M (2010) Numerical study of the free flight characteristics of a flapping wing in low reynolds numbers. AIAA J. Aircraft 47(1):141–150
45. Lani A, Sjögreen B, Yee H, Henshaw W (2013) Variable high-order multiblock overlapping grid methods for mixed steady and unsteady multiscale viscous flows, part ii: hypersonic nonequilibrium flows. Communications in Computational Physics 13(2):583–602
46. Bazilevs Y, Takizawa K, Tezduyar TE (2013) Computational fluid-structure interaction: methods and applications. Wiley, Hoboken
47. De Schepper S, Heynderickx G, Marin G (2009) Modeling the evaporation of a hydrocarbon feedstock in the convection section of a steam cracker. Computers & Chemical Engineering 33(1):122–132
48. De Schepper S, Heynderickx G, Marin G (2008) Cfd modeling of all gas-liquid and vapor-liquid flow regimes predicted by the baker chart. Chem Eng J 138(1–3):349–357
49. Hughes T, Mallet M (1986) A new finite element formulation for computational fluid dynamics: Iv. a discontinuity-capturing operator for multidimensional advective-diffusive systems. Comput Methods Appl Mech Eng 58(3):329–336
50. Tezduyar TE, Senga M (2006) Stabilization and shock-capturing parameters in supg formulation of compressible flows. Comput Methods Appl Mech Eng 195(13–16):1621–1632
51. Bazilevs Y, Hughes TJR (2007) Weak imposition of Dirichlet boundary conditions in fluid mechanics. Computers & Fluids 36:12–26
52. Brooks AN, Hughes TJR (1982) Streamline upwind/Petrov-Galerkin formulations for convection dominated flows with particular emphasis on the incompressible Navier-Stokes equations. Comput Methods Appl Mech Eng 32:199–259
53. Tezduyar TE (1992) Stabilized finite element formulations for incompressible flow computations. Adv Appl Mech 28:1–44
54. Hughes T, Franca L, Hulbert G (1989) A new finite element formulation for computational fluid dynamics?: Viii. the galerkin/least-squares method for advective-diffusive equations,. Comput Methods Appl Mech Eng 73(2):173–189
55. Harari I, Hughes T (1992) What are c and h?: Inequalities for the analysis and design of finite element methods. Comput Methods Appl Mech Eng 97(2):157–192
56. Bazilevs Y, Calo VM, Hughes TJR, Zhang Y (2008) Isogeometric fluid-structure interaction: theory, algorithms, and computations. Comput Mech 43:3–37
57. Takizawa K, Bazilevs Y, Tezduyar TE (2012) Space-time and ALE-VMS techniques for patient-specific cardiovascular fluid-structure interaction modeling. Archives of Computational Methods in Engineering 19:171–225. https://doi.org/10.1007/s11831-012-9071-3
58. Bazilevs Y, Hsu M-C, Takizawa K, Tezduyar TE (2012) ALE-VMS and ST-VMS methods for computer modeling of wind-turbine rotor aerodynamics and fluid-structure interaction. Math Models Methods Appl Sci 22(supp02):1230002. https://doi.org/10.1142/S0218202512300025
59. Bazilevs Y, Takizawa K, Tezduyar TE (2013) Computational Fluid-Structure Interaction: Methods and Applications. Wiley. https://doi.org/10.1002/9781118483565

60. Bazilevs Y, Takizawa K, Tezduyar TE (2013) Challenges and directions in computational fluid-structure interaction. Math Models Methods Appl Sci 23:215–221. https://doi.org/10.1142/S0218202513400010
61. Bazilevs Y, Takizawa K, Tezduyar TE (2015) New directions and challenging computations in fluid dynamics modeling with stabilized and multiscale methods. Math Models Methods Appl Sci 25:2217–2226. https://doi.org/10.1142/S0218202515020029
62. Bazilevs Y, Takizawa K, Tezduyar TE (2019) Computational analysis methods for complex unsteady flow problems. Math Models Methods Appl Sci 29:825–838. https://doi.org/10.1142/S0218202519020020
63. Takizawa K, Tezduyar TE (2012) Computational methods for parachute fluid-structure interactions. Archives of Computational Methods in Engineering 19:125–169. https://doi.org/10.1007/s11831-012-9070-4
64. Takizawa K, Fritze M, Montes D, Spielman T, Tezduyar TE (2012) Fluid-structure interaction modeling of ringsail parachutes with disreefing and modified geometric porosity. Comput Mech 50:835–854. https://doi.org/10.1007/s00466-012-0761-3
65. Takizawa K, Tezduyar TE, Boben J, Kostov N, Boswell C, Buscher A (2013) Fluid-structure interaction modeling of clusters of spacecraft parachutes with modified geometric porosity. Comput Mech 52:1351–1364. https://doi.org/10.1007/s00466-013-0880-5
66. Takizawa K, Tezduyar TE, Boswell C, Tsutsui Y, Montel K (2015) Special methods for aerodynamic-moment calculations from parachute FSI modeling. Comput Mech 55:1059–1069. https://doi.org/10.1007/s00466-014-1074-5
67. Kalro V, Tezduyar TE (2000) A parallel 3D computational method for fluid-structure interactions in parachute systems. Comput Methods Appl Mech Eng 190:321–332. https://doi.org/10.1016/S0045-7825(00)00204-8
68. Zhu Q, Yan J, Tejada-Martínez A, Bazilevs Y (2020) Variational multiscale modeling of langmuir turbulent boundary layers in shallow water using isogeometric analysis. Mech Res Commun 108:103570. https://doi.org/10.1016/j.mechrescom.2020.103570
69. Ravensbergen M, Helgedagsrud TA, Bazilevs Y, Korobenko A (2020) A variational multiscale framework for atmospheric turbulent flows over complex environmental terrains. Comput Methods Appl Mech Eng 368:113182. https://doi.org/10.1016/j.cma.2020.113182
70. Yan J, Korobenko A, Tejada-Martinez AE, Golshan R, Bazilevs Y (2017) A new variational multiscale formulation for stratified incompressible turbulent flows. Computers & Fluids 158:150–156. https://doi.org/10.1016/j.compfluid.2016.12.004
71. Cen H, Zhou Q, Korobenko A (2022) Wall-function-based weak imposition of dirichlet boundary condition for stratified turbulent flows. Computers & Fluids 234:105257
72. Bazilevs Y, Hsu M-C, Akkerman I, Wright S, Takizawa K, Henicke B, Spielman T, Tezduyar TE (2011) 3D simulation of wind turbine rotors at full scale. Part I: Geometry modeling and aerodynamics, International Journal for Numerical Methods in Fluids 65:207–235. https://doi.org/10.1002/fld.2400
73. Takizawa K, Henicke B, Tezduyar TE, Hsu M-C, Bazilevs Y (2011) Stabilized space-time computation of wind-turbine rotor aerodynamics. Comput Mech 48:333–344. https://doi.org/10.1007/s00466-011-0589-2
74. Takizawa K, Henicke B, Montes D, Tezduyar TE, Hsu M-C, Bazilevs Y (2011) Numerical-performance studies for the stabilized space-time computation of wind-turbine rotor aerodynamics. Comput Mech 48:647–657. https://doi.org/10.1007/s00466-011-0614-5
75. Takizawa K, Tezduyar TE, McIntyre S, Kostov N, Kolesar R, Habluetzel C (2014) Space-time VMS computation of wind-turbine rotor and tower aerodynamics. Comput Mech 53:1–15. https://doi.org/10.1007/s00466-013-0888-x
76. Takizawa K, Bazilevs Y, Tezduyar TE, Hsu M-C, Øiseth O, Mathisen KM, Kostov N, McIntyre S (2014) Engineering analysis and design with ALE-VMS and space-time methods. Archives of Computational Methods in Engineering 21:481–508. https://doi.org/10.1007/s11831-014-9113-0
77. Takizawa K (2014) Computational engineering analysis with the new-generation space-time methods. Comput Mech 54:193–211. https://doi.org/10.1007/s00466-014-0999-z
78. Bazilevs Y, Takizawa K, Tezduyar TE, Hsu M-C, Kostov N, McIntyre S (2014) Aerodynamic and FSI analysis of wind turbines with the ALE-VMS and ST-VMS methods. Archives of Computational Methods in Engineering 21:359–398. https://doi.org/10.1007/s11831-014-9119-7
79. Takizawa K, Tezduyar TE, Mochizuki H, Hattori H, Mei S, Pan L, Montel K (2015) Space-time VMS method for flow computations with slip interfaces (ST-SI). Math Models Methods Appl Sci 25:2377–2406. https://doi.org/10.1142/S0218202515400126
80. Otoguro Y, Mochizuki H, Takizawa K, Tezduyar TE (2020) Space-time variational multiscale isogeometric analysis of a tsunami-shelter vertical-axis wind turbine. Comput Mech 66:1443–1460. https://doi.org/10.1007/s00466-020-01910-5
81. Ravensbergen M, Bayram AM, Korobenko A (2020) The actuator line method for wind turbine modelling applied in a variational multiscale framework. Comput Fluids 201:104465. https://doi.org/10.1016/j.compfluid.2020.104465
82. Korobenko A, Hsu M-C, Akkerman I, Bazilevs Y (2013) Aerodynamic simulation of vertical-axis wind turbines. J Appl Mech 81:021011. https://doi.org/10.1115/1.4024415
83. Bazilevs Y, Korobenko A, Deng X, Yan J, Kinzel M, Dabiri JO (2014) FSI modeling of vertical-axis wind turbines. J Appl Mech 81:081006. https://doi.org/10.1115/1.4027466
84. Korobenko A, Bazilevs Y, Takizawa K, Tezduyar TE (2018) Recent advances in ALE-VMS and ST-VMS computational aerodynamic and FSI analysis of wind turbines. In: Tezduyar TE (ed) Frontiers in Computational Fluid–Structure Interaction and Flow Simulation: Research from Lead Investigators under Forty – 2018, Modeling and Simulation in Science, Engineering and Technology. Springer, Berlin, pp 253–336. https://doi.org/10.1007/978-3-319-96469-0_7
85. Korobenko A, Bazilevs Y, Takizawa K, Tezduyar TE (2019) Computer modeling of wind turbines: 1. ALE-VMS and ST-VMS aerodynamic and FSI analysis, Archives of Computational Methods in Engineering 26:1059–1099. https://doi.org/10.1007/s11831-018-9292-1
86. Bayram AM, Bear C, Bear M, Korobenko A (2020) Performance analysis of two vertical-axis hydrokinetic turbines using variational multiscale method. Comput Fluids 200:104432. https://doi.org/10.1016/j.compfluid.2020.104432
87. Yan J, Korobenko A, Deng X, Bazilevs Y (2016) Computational free-surface fluid-structure interaction with application to floating offshore wind turbines. Comput Fluids 141:155–174. https://doi.org/10.1016/j.compfluid.2016.03.008
88. Yan J, Deng X, Xu F, Xu S, Zhu Q (2020) Numerical simulations of two back-to-back horizontal axis tidal stream turbines in free-surface flows. Journal of Applied Mechanics 87(6). https://doi.org/10.1115/1.4046317
89. Kuraishi T, Zhang F, Takizawa K, Tezduyar TE (2021) Wind turbine wake computation with the st-vms method, isogeometric discretization and multidomain method: I. computational framework. Comput Mech 68(1):113–130
90. Kuraishi T, Zhang F, Takizawa K, Tezduyar TE (2021) Wind turbine wake computation with the st-vms method, isogeometric discretization and multidomain method: Ii. spatial and temporal resolution,. Comput Mech 68(1):175–184

91. Ravensbergen M, Mohamed A, Korobenko A (2020) The actuator line method for wind turbine modelling applied in a variational multiscale framework. Computers & Fluids 201:104465
92. Mohamed A, Bear C, Bear M, Korobenko A (2020) Performance analysis of two vertical-axis hydrokinetic turbines using variational multiscale method. Computers & Fluids 200:104432
93. Bayram A, Korobenko A (2020) Variational multiscale framework for cavitating flows, Computational Mechanics 1–19
94. Yan J, Deng X, Korobenko A, Bazilevs Y (2017) Free-surface flow modeling and simulation of horizontal-axis tidal-stream turbines. Comput Fluids 158:157–166. https://doi.org/10.1016/j.compfluid.2016.06.016
95. Zhu Q, Yan J (2021) A moving-domain CFD solver in FEniCS with applications to tidal turbine simulations in turbulent flows. Computers & Mathematics with Applications 81:532–546
96. Bayram AM, Korobenko A (2020) Variational multiscale framework for cavitating flows. Comput Mech 66:49–67. https://doi.org/10.1007/s00466-020-01840-2
97. Cen H, Zhou Q, Korobenko A (2021) Variational multiscale framework for cavitating flows. Computers & Fluids 214:104765. https://doi.org/10.1016/j.compfluid.2020.104765
98. Codoni D, Moutsanidis G, Hsu M-C, Bazilevs Y, Johansen C, Korobenko A (2021) Stabilized methods for high-speed compressible flows: toward hypersonic simulations. Comput Mech 67:785–809. https://doi.org/10.1007/s00466-020-01963-6
99. Terahara T, Takizawa K, Tezduyar TE, Bazilevs Y, Hsu M-C (2020) Heart valve isogeometric sequentially-coupled FSI analysis with the space-time topology change method. Comput Mech 65:1167–1187. https://doi.org/10.1007/s00466-019-01813-0
100. Hsu M-C, Kamensky D, Bazilevs Y, Sacks MS, Hughes TJR (2014) Fluid-structure interaction analysis of bioprosthetic heart valves: significance of arterial wall deformation. Comput Mech 54:1055–1071. https://doi.org/10.1007/s00466-014-1059-4
101. Johnson EL, Wu MCH, Xu F, Wiese NM, Rajanna MR, Herrema AJ, Ganapathysubramanian B, Hughes TJR, Sacks MS, Hsu M-C (2020) Thinner biological tissues induce leaflet flutter in aortic heart valve replacements. Proc Natl Acad Sci 117:19007–19016
102. Takizawa K, Bazilevs Y, Tezduyar TE, Hsu M-C (2019) Computational cardiovascular flow analysis with the variational multiscale methods. Journal of Advanced Engineering and Computation 3:366–405. https://doi.org/10.25073/jaec.201932.245
103. Kuraishi T, Terahara T, Takizawa K, Tezduyar T (2022) Computational flow analysis with boundary layer and contact representation: I. tire aerodynamics with road contact. J Mech 38:77–87
104. Terahara T, Kuraishi T, Takizawa K, Tezduyar T (2022) Computational flow analysis with boundary layer and contact representation: Ii. heart valve flow with leaflet contact,. J Mech 38:185–194
105. Otoguro Y, Takizawa K, Tezduyar TE, Nagaoka K, Avsar R, Zhang Y (2019) Space-time VMS flow analysis of a turbocharger turbine with isogeometric discretization: Computations with time-dependent and steady-inflow representations of the intake/exhaust cycle. Comput Mech 64:1403–1419. https://doi.org/10.1007/s00466-019-01722-2
106. Otoguro Y, Takizawa K, Tezduyar TE, Nagaoka K, Mei S (2019) Turbocharger turbine and exhaust manifold flow computation with the Space-Time Variational Multiscale Method and Isogeometric Analysis. Computers & Fluids 179:764–776. https://doi.org/10.1016/j.compfluid.2018.05.019
107. Xu F, Moutsanidis G, Kamensky D, Hsu M-C, Murugan M, Ghoshal A, Bazilevs Y (2017) Compressible flows on moving domains: Stabilized methods, weakly enforced essential boundary conditions, sliding interfaces, and application to gas-turbine modeling. Computers & Fluids 158:201–220. https://doi.org/10.1016/j.compfluid.2017.02.006
108. Takizawa K, Tezduyar TE, Kuraishi T (2015) Multiscale ST methods for thermo-fluid analysis of a ground vehicle and its tires. Math Models Methods Appl Sci 25:2227–2255. https://doi.org/10.1142/S0218202515400072
109. Kuraishi T, Takizawa K, Tabata S, Asada S, Tezduyar TE (2014) Multiscale thermo-fluid analysis of a tire. In: Proceedings of the 19th Japan Society of Computational Engineering and Science Conference, Hiroshima, Japan
110. Takizawa K, Tezduyar TE, Kuraishi T (2016) Flow analysis around a tire with actual geometry, road contact and deformation, in preparation
111. Kuraishi T, Takizawa K, Tezduyar TE (2018) Space–time computational analysis of tire aerodynamics with actual geometry, road contact and tire deformation. In: Tezduyar TE (ed) Frontiers in Computational Fluid–Structure Interaction and Flow Simulation: Research from Lead Investigators under Forty – 2018, Modeling and Simulation in Science, Engineering and Technology. Springer, Berlin, pp 337–376. https://doi.org/10.1007/978-3-319-96469-0_8
112. Kuraishi T, Takizawa K, Tezduyar TE (2019) Tire aerodynamics with actual tire geometry, road contact and tire deformation. Comput Mech 63:1165–1185. https://doi.org/10.1007/s00466-018-1642-1
113. Kuraishi T, Takizawa K, Tezduyar TE (2019) Space-time computational analysis of tire aerodynamics with actual geometry, road contact, tire deformation, road roughness and fluid film. Comput Mech 64:1699–1718. https://doi.org/10.1007/s00466-019-01746-8
114. Yan J, Korobenko A, Deng X, Bazilevs Y (2016) Computational free-surface fluid-structure interaction with application to floating offshore wind turbines. Computers & Fluids 141:155–174
115. Hsu M, Akkerman I, Bazilevs Y (2012) Wind turbine aerodynamics using ALE-VMS: Validation and the role of weakly enforced boundary conditions. Comput Mech 50(4):499–511
116. Zhu Q, Yan J (2021) A mixed interface-capturing/interface-tracking formulation for thermal multi-phase flows with emphasis on metal additive manufacturing processes. Comput Methods Appl Mech Eng 383:113910
117. Liu J, Lan I, Tikenogullari O, Marsden A (2021) A note on the accuracy of the generalized-α scheme for the incompressible navier-stokes equations. Int J Numer Meth Eng 122(2):638–651